Global Structure and Dynamics of Human Apolipoprotein CII in Complex with Micelles: Evidence for Increased Mobility of the Helix Involved in the Activation of Lipoprotein Lipase[†,‡]

J. Zdunek,[§] G. V. Martinez,[§] J. Schleucher,[§] P. O. Lycksell,[§] Y. Yin,[¶] S. Nilsson,[¶] Y. Shen,[¶] G. Olivecrona,[¶] and S. Wijmenga*,[§,#]

Department of Medical Biochemistry and Biophysics and Medical Biosciences, Physiological Chemistry, Umeå University, SE-901 87 Umeå, Sweden

Received August 23, 2002; Revised Manuscript Received December 17, 2002

ABSTRACT: Apolipoprotein CII (apoCII), a surface constituent of plasma lipoproteins, is the activator for lipoprotein lipase (LPL) and is therefore central for lipid transport in blood. The three-dimensional structure of ^{13}C-, ^{15}N-enriched human full-length apoCII in complex with sodium dodecyl sulfate (SDS) micelles is reported. In addition to the structure determination, ^{15}N-relaxation measurements have been performed at two magnetic fields to characterize the dynamics of the backbone of apoCII in the complex. The relaxation data also provided global structural constraints, viz. the orientation of helices in the complex. In addition, global constraints were derived from the fact that apoCII helices are attached to the surface of the SDS micelle and that the hydrophobic moments of each helix faces the interior of the micelle. These three categories of global constraints, together with the local classical NMR constraints, were sufficient to define the 3D structure of the apoCII−SDS micelle complex. To our knowledge, this presents the first example in which the global structure of a protein−SDS micelle complex has been determined. The C-terminal helix of apoCII is known to be responsible for the activation of LPL. This helix is distinguished from the other helices by a higher degree of internal motion on the nanosecond time scale as shown by the relaxation data. The overall structure and the internal dynamics, combined with previous mutation data, give important clues toward a possible mechanism for the activation of LPL by apoCII.

Apolipoproteins (apo's) are important constituents of the plasma lipoproteins (*1*, *2*). Some apolipoproteins are necessary for the intracellular lipoprotein assembly (apoB100 and apoB48), some are ligands for interaction between lipoproteins and receptors (apoB, apoE), some are activators for enzymes involved in lipoprotein turnover (apoAI and apoCII), while others act as modulators of the mentioned processes (apoCIII, apoCI, apoAII, and others). Apolipoprotein CII (apoCII) was the first apolipoprotein for which a specific function was found, namely, that it activates the enzyme lipoprotein lipase (LPL)[1] (*3*). A lack of functional apoCII leads to severe hypertriglyceridemia, similar to what is seen for a genetic deficiency of the enzyme itself (*4*).

All apolipoproteins, with the exception of the very large apoB, are able to move between different lipoprotein particles and thus belong to the group of exchangeable apolipoproteins (*2*, *5*). They contain one or several amphipathic helices, early identified by secondary structure prediction programs, and important for the reversible interaction with lipids. Until now, only one full-length apolipoprotein, apolipophorin III from the insect *Locust migratoria*, has been crystallized and structurally determined to high resolution (*6*). Structural data at 4 Å resolution are also available for the major part of human apoAI (apoAIΔ1−43) (*7*). In addition, structures of synthetic and recombinant peptides from several apolipoproteins have been determined by crystallography and by NMR (apoE, apoAI, apoAII, and apoCI) (*8*−*14*).

Human apoCII consists of 79 amino acid residues. Amphipathic helices were predicted for residues 14−39, 43−55, and 60−76 (*2*). Previous studies in vitro, with synthetic lipid substrates and synthetic fragments of apoCII, have shown that the structures needed for activation of LPL reside in the C-terminal one-third of the apoCII molecule (*15*), while lipid binding seemed to be confined to fragments from the N-terminal 2/3 (*16*). With natural lipid substrates (apoCII-deficient chylomicrons), lipid-binding of the N-terminal part was needed for efficient activation (*17*). Sequence comparisons of apoCII from 10 different vertebrate species, from fish to man, revealed that the N-terminal two-thirds of the amino acid sequence differs very much between

---

[†] This research was supported by grants from the Natural Science Research Council (S.W.), the Medical Research Council (G.O., nos. 727 and 12293), and the Fund for Research in Biotechnology at Umeå University (S.W. and G.O.).

[‡] Structures and NMR restraints have been deposited in the Protein Data Bank under accession codes 1o8t and 1o8tmr, respectively.

* Correspondence to: Prof. Dr. Sybren S. Wijmenga, Lab. of Biophysical Chemistry, University of Nijmegen, Toernooiveld 1, 6525ED Nijmegen, The Netherlands. E-mail: sybren.wijmenga@chem.umu.se. Phone: +31-243652678. Fax: 31-243652112.

[§] Department of Medical Biochemistry and Biophysics.

[¶] Department of Medical Biosciences.

[#] Present address: Lab. of Biophysical Chemistry, University of Nijmegen, Toernooiveld 1, 6525ED Nijmegen, The Netherlands.

[1] Abbreviations: LPL: lipoprotein lipase, SDS: sodium dodecyl sulfate, DSS: 4,4-dimethyl 4-silapentate sodium carboxylate, NOE: nuclear overhauser enhancement, NMR: nuclear magnetic resonance

10.1021/bi0267184 CCC: $25.00

apoCII from mammals and other vertebrates (chicken or fish). However, the amphipathic nature seemed to be conserved, although there were almost no sequence identities (*18*, *19*). In contrast, in the C-terminal one-third of apoCII, seven fully conserved residues were identified (*19*). Their role for activation was studied by site-directed mutagenesis (*20*). It was found that the four most crucial residues were all located on the same face of a putative α-helix and could represent a potential binding site for LPL (*20*). In previous studies by some of us, the solution structure of the apoCII fragment 50−79 in hexafluoropropanol was studied by ^{1}H NMR (*21*, *22*). This demonstrated helix formation in the sequence regions 56−59 and 67−74. Later a study of the apoCII fragment 44−79 in the presence of micelles of sodium dodecyl sulfate (SDS) demonstrated a similar helical structure (*23*). Furthermore, it was shown that apoCII under certain conditions may self-aggregate to fibrils in a fashion resembling amyloid (*24*).

We describe here NMR studies of the three-dimensional structure and dynamics of ^{13}C-, ^{15}N-enriched, human full-length apoCII in complex with SDS micelles. Initial experiments with full-length apoCII demonstrated that the high content of α-helices made assignments of individual residues difficult because of overlapping NMR signals. In addition to NMR experiments for structure determination, relaxation measurements have been performed at two magnetic fields to characterize the dynamics of apoCII in the complex with SDS micelles. The relaxation data also provided global structure information, which together with the classical NMR constraints, was sufficient to define the 3D structure of the apoCII−SDS micelle complex. To our knowledge, this presents the first example in which the global structure of a protein−SDS micelle complex has been determined. The overall structure and the internal dynamics combined with the previous mutation data reported by some of us (*20*) give important clues toward a possible mechanism for the activation of LPL by apoCII. During the course of our work, MacRaild et al. (*25*) reported an NMR structure of full-length apoCII based on classical NMR constraints (NOEs and *J*-couplings), using single isotope enrichment (^{15}N). However, these classical NMR constraints do not define the global structure, and the dynamics of the complex was not studied.

MATERIALS AND METHODS

ApoCII Expression. cDNA for human apolipoprotein CII (hapoCII, originally a kind gift from Dr. Steven Humphries, London) was connected to an EcoRI linker coding for the cleavage site for Factor Xa attached to the first codon of the mature apoCII cDNA sequence. The whole DNA fragment was cloned into the EcoRI/XhoI site of the vector pET29a-(+) (Novagen Inc., Madison, WI) to form the expression plasmid pET29a-hapoCII. The recombinant was verified by EcoRI/XhoI cleavage and DNA sequencing. The plasmid was transformed into *Escherichia coli* BL21(DE3) to express the fusion protein S-tag-“factor Xa cleavage site”-hapoCII (117 amino acid residues in total). Expression was made in 2 L of M9 special medium with 1.01 g of $^{15}NH_4Cl$ and 6.02 g of ^{13}C-glucose. At an A_{600} of 1.2, induction was started by addition of 0.5 mM IPTG. After 30 min at 37 °C followed by 30 min on ice, the bacteria were pelleted by low speed centrifugation and the pellet was mixed with 100 mL of 8 M urea, 0.15 M NaCl, 0.1% Triton X-100, 0.1% SDS, 20 mM Tris-Cl, pH 7.4. After the sample was homogenized, the suspension was left on a shaker at room temperature overnight. After centrifugation of the sample and recovery of the extract, the remaining pellet was extracted twice more in 50 mL of the urea-containing buffer. The three supernatants were combined and diluted with 3 volumes of 0.1% Triton X-100, 0.15 M NaCl, 20 mM Tris-Cl, pH 7.2, so that the final urea concentration was 2 M. The fusion protein was then slowly applied to a 14 mL column of S-protein Agarose (Novagen Inc.). After the column was washed with 2 M urea, 0.15 M NaCl, 20 mM Tris-Cl, until the absorbance of the eluate was down to zero, elution was made with 2 M guanidine thiocyanate (GTC) in the same buffer. Fractions containing protein were collected (together about 13 mL) and then extensively dialyzed against 1 M urea, 0.1 M NaCl, 2 mM $CaCl_2$, 20 mM Tris-Cl, pH 8.0 at 4 °C (for 3 days). The procedure was repeated once with the pass through volume, containing unbound material from the first column. This material was applied once again to the column and eluted and dialyzed as described.

Cleavage of Fusion Protein and Purification. The combined eluates from the S-protein agarose (31.7 mL, $A_{280} = 0.28$) was treated with 0.175 mg of bovine factor Xa (New England BioLabs, Beverly, MA) for 67 h at room temperature. The material was again applied to the S-protein Agarose (flow rate = 25 mL/h). The pass through was collected (49 mL, $A_{280} = 0.13$, protein analysis with BCIP Pierce = 0.083 mg/mL) and dialyzed extensively against 10 mM ammonium bicarbonate at 4 °C. The sample was then lyophilized generating 5.5 mg of dry powder.

Electrophoresis, N-Terminal Amino Acid Sequence Analyses and Activation Assay. The purification was in all steps followed by SDS−PAGE on Tricine gels stained with Serva Blue (*18*). ApoCII immunoreactivity was localized by Western blotting using a rabbit anti-human apoCII antiserum (produced against apoCII purified from human plasma and covalently bound to keyhole limpet hemocyanin using glutaraldehyde). Cleavage of the fusion protein was complete after 67 h, but N-terminal sequence analyses revealed that the main part of the material was lacking the first N-terminal Thr−Gln residues. Some material lacking the first Thr residue (starting at Gln−Gln−Asp−Glu−Met) was also found. Experiments with shorter cleavage time with factor Xa gave intact N-terminal sequence, but less complete cleavage of the fusion protein (data not shown). In an activation assay for LPL, using an emulsion of soybean triglycerides with a trace amount of [^{3}H]-oleoyl-labeled triolein in 10 mg of egg yolk phospholipids (*20*), both the fusion protein and the product isolated after cleavage with factor Xa were able to activate LPL to the same level as apoCII purified from human plasma did (data not shown).

NMR. (a) Preparation of Sample for Analyses by NMR. The lyophilized, isotope-labeled sample was dissolved in 0.5 mL of 5 M urea, 10 mM Tris-Cl, pH 8.5. SDd25-S was added to a concentration of 200 mM (31.3 mg) and the solution was left at room temperature for 2 h. It was then dialyzed against 10 mM SDd25-S and 10 mM deuterated acetic acid in H_2O (pH 5.0) with three changes during 48 h (dialysis tube with MW cut off 3500). For the final NMR sample, ^2H_2O was added to 10% volume percent solution and the SDS concentration was increased to 380 mM SDd25-S(pH 5.0). A temperature series of ^{1}H, ^{15}N HSQC spectra were

Table 1: NMR Experiments Used to Assign and Analyze the $^{1}H/^{15}N/^{13}C$ Resonances in the ApoCII−SDS Micelle Complex

dimension	^{1}H (acquisition, D3)			D2				D1						
experiment[a]	SW[b] (ppm)	N[c]	Car[d] (ppm)	Nuc[e]	SW[b] (ppm)	N[c]	Car[d] (ppm)	Nuc[e]	SW[b] (ppm)	N[c]	Car[d] (ppm)	processed size[f]	no. of scans[g]	mixing time[h] (ms)
CBCANH[i,m]	8.33(4.2)	1024	8.00	15N	20	54	116.0	13C	61	112	43.5	512/128/512	32	
CBCACONH[i,n]	4.41(4.2)	768	8.00	15N	20	54	116.0	13C	61	112	43.5	512/128/256	16	
CBCACONH[i,n]	11.87	1536	4.71	13C	8.00	54	175	13C	60	110	43.5	1024/256/512	24	
SlHCANH[j]	8.75	1024	8.79	15N	19	54	119	13C	25	162	52.5	1024/512/512	32	
HCCCONH[k]	12.67	1024	5.00	15N	19	42	118.5	13C	64	128	39	2048/128/1024	48	13.2
HNCO[i]	8.01	1024	8.00	15N	20.0	64	119	13C	8	128	175	1024/256/512	4	
15N−NOESY−HSQC[i]	9.90	1024	8.00	1H	8.86	148	4.71	15N	19.0	112	119	256/1024/512	16	120
13C−NOESY−HSQC[i]	8.98	1024	4.71	1H	8.86	148	4.71	13C	47.2	128	41.4	1024/256/512	16	120
HNHA[l]	11.97	2048	4.71	1H	8.50	100	4.71	15N	22.1	92	118.0	2048/256/512	16	

[a] NMR experiments for assignment and data extraction. All experiments were recorded at 600 MHz ^{1}H frequency, except the HCCCONH, which was recorded at 500 MHz. The frequency-labeled nuclei are underlined. In the CBCACONH the ^{15}N carrier was set at 118.0 ppm. [b] SW: sweep width (between brackets SW after processing). [c] N: number of real data points recorded. [d] Carrier: carrier position. [e] Nuc: active nucleus. [f] Processed size: size of data matrix after processing. [g] Number of scans recorded per free induction decay. [h] Mixing time of NOESY or carbon−carbon TOCSY. [i] The experiments use gradient enhancement (Kay et al. (*30*); Schleucher et al. (*31*)). [j] Larsson et al. (*32*). [k] Montelione et al. (*33*). [l] Vuister et al. (*34*). [m] Ref *35*. [n] Ref *36*.

obtained at 380 mM SDS concentration to determine the optimal experimental temperature, which turned out to be 40 °C, as found in other cases (*26*). The relatively high SDS concentration was chosen to reduce the possibility of apoCII self-association on the micelle surface (*27*). With a final 0.5 mM apoCII concentration and ca. 60 SDS molecules per micelle, there is about 1 apoCII molecule per 12 SDS micelles. This was higher than the ratio of ca. 1:2 used by MacRaild et al. (*25*).

(b) Resonance Assignment and Structural Parameters. Table 1 summarizes the NMR experiments used for resonance assignments, extraction of J-coupling data and NOE data. All NMR experiments were recorded at a temperature of 40 °C on the 0.5 mM $^{13}C/^{15}N$ double-labeled apoCII in complex with SDS micelles (see above). The spectral data were analyzed using UXNMR and/or XEASY (*28*). The assignment of the backbone resonances was achieved via standard triple-resonance methods (for a recent review see ref *29*) using the following set of triple-resonance experiments: CBCANH, CBCA(CO)NH, CBCACO(N)H, HNCO, and slHCANH (spin-locked HCANH) (Table 1). The Cα and Cβ resonance assignment were confirmed by the side-chain directed HCC(CO)NH experiment. The H_N and H_α proton assignment were confirmed by the $^{1}H/^{15}N$−NOESY−HSQC and/or NOESY experiments. NOEs were measured via the $^{1}H/^{15}N$−NOESY HSQC (120 ms mixing time) and/or NOESY experiments (Table 1). Although ^{13}C-edited NOESY experiments were carried out, no reliable identification of interresidue side-chain NOEs could be achieved. The $^{3}J_{H\alpha HN}$-couplings were measured with the HNHA experiment (Table 1).

(c) NMR Relaxation Measurements. The ^{15}N-relaxation measurements were carried out as described by Larsson et al. (*37*). Briefly, the longitudinal (T_1) and transverse (T_2) ^{15}N-spin relaxation times were measured at 400 and 600 MHz ^{1}H frequency (40.5 and 60.8 MHz ^{15}N frequency) using the standard pulse sequences proposed by Farrow et al. (*38*). The delays for ^{15}N relaxation were varied nonlinearly, to achieve an optimal determination of the relaxation times (*39*). For each experiment, the data points were recorded in an interleaved manner with the relaxation delays randomly distributed. The heteronuclear ^{15}N-$\{^{1}H\}$ NOE experiment was measured three times at 600 MHz and twice at 500 MHz. Before the start of each experiment, the temperature was calibrated with a water/DSS sample (DSS: 4,4-dimethyl 4-silapentate sodium carboxylate). The carrier was set in the middle of the amide region, i.e., 8.00 and 118.0 ppm for ^{1}H and ^{15}N, respectively.

At 600 MHz, the ^{15}N T_1 spectra had relaxation delays of 5*, 401, 502, 602, 702, 802, 902, 1003, and 1204 ms (* duplicate time points). The ^{15}N T_2 experiments were recorded with relaxation delays of 16*, 31, 47, 62*, 93*, and 125* ms. The delay δ of the δ-180-δ block of the CPMG sequence was set to 450 μs. At 400 MHz, the ^{15}N T_1 experiments were measured with relaxation delays of 5*, 400, 450, 500, 600, 700, 800, 900, and 1000 ms. The T_2 experiments were recorded with relaxation delays of 7*, 36, 43, 72*, 79, 108, 115, and 130 ms with the delay between the 180° pulses in the CPMG sequence set to 450 μs. Relatively long relaxation delays between scans of 1.6 s were employed in all the ^{15}N T_1 and T_2 experiments.

In the measurements of the heteronuclear ^{15}N-$\{^{1}H\}$ NOE, a pulse sequence with water flip-back was used (*40*), to minimize the effect of the slowly relaxing water magnetization on the NOE measured from amides with rapidly exchanging protons. The water signal was suppressed by a water-gate pulse sequence (*41*). NOE values were determined from pairs of spectra recorded with and without proton saturation. The two spectra were recorded in an interleaved manner analogous to the T_1 and T_2 measurements, with the spectrum in the absence of proton saturation as the first experiment. Proton saturation was achieved by application of 120° pulses every 5 ms. Spectra recorded with proton saturation utilized a 4 s period of saturation, whereas the spectra recorded without saturation had a 4 s recovery delay.

(d) NMR Relaxation Analysis. All relaxation data spectra were analyzed using SYBYL software (TRIPOS), using a small integration area encompassing only the top of the peak as described by Larsson et al. (*37*). The use of such small integration area has the advantage that the noise is still averaged, while at the same time partially overlapping cross-peaks can be reliably integrated. This leads to more accurate T_1 and T_2 data (*42*). The relaxation times T_1 and T_2 were extracted by fitting a single-exponential decaying function to the measured decay curves using home-written Matlab scripts. The error in the T_1 and T_2 values was estimated by

performing the curve fitting first with a data set containing all 10 time points and then with two reduced data sets, containing only every second time point in the relaxation series (*37*). The errors in T_1 and T_2 were calculated as the standard deviation between these different curve fittings. The steady-state NOE values were determined from the ratios of the peak volumes from spectra recorded in the presence and absence of proton saturation. The standard deviations of the NOE values were determined from the weighed average of the NOE values from the five measurements (600 and 500 MHz). Finally, the measured NOE was corrected for incomplete magnetization recovery during the 4 s long relaxation delay according to Grzesiek and Bax (*40*).

The T_1, T_2, and NOE data measured at two fields were then analyzed using the home-written software PINATA, which is written in Matlab scripts (*43*). This analysis makes it possible to unambiguously establish whether there are contributions from the picosecond time scale as well as nanosecond time scale internal motions, by focusing on the field dependence of the relaxation times. The apparent overall-tumbling time ($\tau_m^{\circ,app}$) of each N−H vector is derived from T_1/T_2 ratios. Using its field dependence, $\tau_m^{\circ,app}$ is corrected for nanosecond time scale internal motion giving τ_m° and by using their field dependence the T_2's are corrected for exchange broadening. The latter also gives the exchange broadening R_{ex}. These corrections are performed simultaneously in an iterative manner. In this way the residue-specific overall tumbling time (τ_m°) can be determined irrespective of the time scale of internal motion. It is then possible to derive the rotational diffusion tensor, which follows from the distribution of τ_m°, even for molecules or complexes where many residues are affected by nanosecond time scale motion. As a final step in the analysis, the squared order parameters and time scales for internal motion are determined via fitting.

From the rotational diffusion tensor and the effective rotation correlation time of a residue one can derive the orientation of the N−H vector in the molecular frame (*43*). In the absence of internal motion, for small degrees of anisotropy, and axial symmetry τ_m° can to good approximation be written as (*43*)

$$\tau_m^{\circ} = \tau_l^{\circ}/\left(1 + \frac{\Delta}{2}\sin^2(\Phi)\right) \qquad (1)$$

Here, Δ is well approximated by $\Delta = (\tau_l^{\circ}/\tau_s^{\circ}) - 1 = (D_{\|}/D_{\perp}) - 1)$ where $\tau_l^{\circ} (= (6D_{\perp})^{-1})$ is the tumbling of the symmetry axis of the diffusion tensor and τ_s° $(= (6D_{\|})^{-1})$ represents the tumbling of the perpendicular axes. Thus, for small anisotropies, τ_m° contains structure information, namely, on the angle Φ each relaxation vector (N−H vector) makes with the symmetry axis of the diffusion tensor. Furthermore, as follows from eq 1, when $\Phi = 0$, τ_m° attains its maximum value, $\tau_m^{\circ,max}$, which is equal to τ_l°. When $\Phi = 90°$, τ_m° attain its minimum value $\tau_m^{\circ,min}$ which is equal to $\tau_l^{\circ}/(1 + (\Delta/2))$. Both values can be estimated from the experimentally observed distribution of τ_m° values. Subsequently, from their ratio Δ and thus the anisotropy of the diffusion tensor ($D_{\|}/D_{\perp}$) can simply be calculated from

$$D_{\|}/D_{\perp} = (2((\tau_m^{\circ,max}/\tau_m^{\circ,min}) - 1)) + 1 \qquad (2)$$

Structure Calculations. (a) Strategy. Structure calculations of apoCII in complex with SDS micelles were performed in two parts. In part I, a standard simulated annealing protocol was applied to derive a set of structures based on "classical" NMR constraints. In part II, a protocol was developed and applied to derive the "globally" defined structure of the complex using three types of additional "global" constraints (see below). All calculations were carried out in XPLOR vs 3.851 (*44*). The final structures and intermediate results were displayed via the VMD program (*75*).

(b) Part I, Structure Calculations using Classical NMR Constraints. (i) Distance Constraints. ^{15}N-edited NOESY spectra (as described in NMR Experiments) were used to extract the experimental intensities of cross-peaks between protons. Distance constraints were evaluated from the experimental intensities using the complete relaxation matrix algorithm program MARDIGRAS to take into account the effects of spin diffusion (*45*). In total, 118 distances were obtained in this way. The ranges of the distances proposed by MARDIGRAS were tighter than seemed realistic. Therefore, new lower and upper distance bounds were calculated for every distance according to Folmer et al. (*46*), so that MD calculations could be performed. The average value of upper and lower bounds was 0.664 Å. Additionally, we have used 118 distances that corresponded to the observable peaks in the spectra, but for which we could not calculate intensities because of the complicated spectra. For those distances we have assigned a uniform value of 3.5 Å with the large ranges ± 1.5 Å. In total, we have used 236 distance constraints. The distances were operationally divided in six groups: HA(i)−HN(i+1), 54 distances; HA(i)−HN(i+2), 37 distances; HA(i)−HN(i+3), 31; HA(i)−HN(i+4), 28 distances; HN(i)−HN(i+1), 56 distances; and HN(i)−HN(i+2), 30 distances. Because of overlap and overall complexity of the NMR spectra obtained for the system (protein and micelle), no distance constraints involving side-chain protons were included in the calculations.

(ii) Torsion Angle Constraints. The constraints on ϕ and ψ backbone torsion angles were derived using C^{α} chemical shift indices as described in Wishart et al. (*47*). For those residues for which the chemical shift indicated an α-helical conformation, the ϕ and ψ torsion angles were kept at canonical −58° and −47°, respectively, with the ranges ± 30°. No torsion angle constraints derived from C^{α} chemical shift indices were used for the residues 1−14, 28, 38−43, 48, 52, and 76−79. Additionally, 56 J_{HNHA}-coupling constants obtained from NMR measurements were used directly in the XPLOR force field for constraining ϕ torsion angles of the backbone.

(iii) Generation of apoCII Starting Structures. The starting model of apoCII was generated in α-helix conformation along the whole sequence from residues 1 to 79 using the module BIOPOLYMERS of the program SYBYL. The coordinates of the apoCII model were then converted to the form suitable for the program XPLOR. The hydrogen atoms were built in using XPLOR and the model was energy minimized using 1000 step of Powell minimization algorithm.

(iv) Simulated Annealing Protocol. From the apoCII starting structure and using the classical NMR constraints, the simulated annealing (SA) algorithm of the XPLOR program (version 3.851) (*44*, *48*) was used to generate 100

structures of apoCII. The SA algorithm was used as delivered with the program, but with modifications of the lengths and temperatures of the high-temperature and cooling periods: The high-temperature period was set to 36000 steps at 2000 K, and the cooling period to 24000 steps. The temperature for the cooling period was lowered gradually in steps from initial 2000 to 100 K. The integration step of the molecular dynamics run was set to 1 fs. The resulting (from SA calculations) 100 structures of apoCII were energy minimized using 1000 steps of Powell minimization algorithm.

(c) Part II, Structure Calculations using "Global" NMR Constraints. (i) Final Global Structure Calculation Protocol (*Brief Description*). The final structure calculation protocol using both "global" and "classical" constraints worked as follows. Each structure from the set of 100 structures obtained using classical NMR constraints was read into XPLOR. The structure was segmented into four parts, namely, segment 1a (residues 1−27), segment 1b (residues 28−42), segment 2 (residues 43−62), and segment 3 (residues 63−79). The helices for the respective segments were assigned for segment 1a (residues 16−26), segment 1b (residues 29−38), segment 2 (residues 45−58), and segment 3 (residues 64−74). A helical axis and a hydrophobic moment were calculated for each helix (see Determination of Helical Axes and Hydrophobic Moment Calculations). Then each segment was oriented via rigid body rotations in XPLOR with its helix axis on a cone. The cone-half angles follow from the helix orientation angles derived from the relaxation data. They correspond to the orientation of the helix axes with respect to the long axis of the diffusion tensor (case c, Results). The molecular coordinate system was defined in such a way that the long axis of the diffusion tensor corresponds to the *z*-axis of the molecular coordinate system. In addition, the segments were faced, via rigid body rotations around the corresponding helix axes, with the hydrophobic moments of the helices (see Hydrophobic Moment Calculations) pointing toward the center of the micelle. Also, the segments were placed via translation at a SDS micelle radius distance from the center of the micelle (see Generation of the SDS Micelle Structure). The separation between residues 38 and 45 (end of helix 1b and start of helix 2, respectively) was kept equal to the average distance between these residues calculated from the 100 structures (≈11 Å). A similar procedure was used for the connection between the other segments. After orienting, facing, and placing of the helices, the C^{α} atoms on both ends of each helix were kept fixed and the whole structure was refined using the MD simulated annealing protocol and energy minimized. During the final minimization we used the "classical" NMR constraints only (distances and torsion angle constraints). Using this procedure, we obtained our final structures. The protocol is available on request.

(ii) Final Global Structure Calculation Protocol (*Orienting and Facing of Helices on Surface of Micelle, Technical*). The final protocol started with reading into XPLOR the coordinates of an individual structure obtained from the previous restrained MD calculations using classical constraints. To manage a helix (start, end) and its hydrophobic moment (start, end) individually, a set of four temporary atoms (belonging to a temporary segment) was defined. As described above the molecule was split into four segments with associated helices. An algorithmic switch in the protocol was implemented to treat the four helical parts (segments) separately. A copy of the original coordinates of each helical part of apoCII was created and merged together with the four temporary (empty as yet) atoms to form a new topological structure. Segment 1 was translated and rotated so that the principal axis system of the associated helix coincided with the xyz-axes as defined in XPLOR. The modules to calculate the helical axis (see Determination of Helical Axes) and the hydrophobic moment (see Hydrophobic Moment Calculations) were invoked and an array of the four temporary atoms was filled with the coordinates. Two temporary atoms kept the coordinates of the beginning and end of the helical axis. The remaining two atoms were filled with the coordinates representing the start (middle of the helix axis) and the end of the calculated hydrophobic moment scaled to a length equal to the radius of the micelle (22.44 Å, see Generation of the SDS Micelle Structure). Via rotation (and translation) the helical long axis was oriented to coincide with the *z*-axis keeping the helix middle centered at the origin. The whole system was then translated and rotated so that the hydrophobic moment vector lay along the *x*-axis with its end point at the origin. The last operation ensured that the helix axis of the segment would stay on the surface of the micelle and meets the requirement that the hydrophobic moment points to the center of the micelle. In this way, the segments can now conveniently be rotated over the surface of the micelle. All other segments were prepared in the same way. The final parts of the protocol were to orient helical axes of the respective segments to agree with the experiment (i.e., the helix orientation derived from relaxation data, see Results) taking into account the possibility of different cases (degeneracy of orientations, see Results). At the same time, the distance between end point of a helix and beginning point of the consecutive second helix was checked, to preserve the covalent connectivity of the molecule. The protocol allows also for corrections (small translations and rotations around different axes) before performing final optimization of the loops (junctions between consecutive segments), using restrained molecular dynamics.

(iii) Generation of the SDS−Micelle Structure. The all-atom model of individual SDS molecules was created within XPLOR, with partial charges on the atoms and other parameters taken as in the all-hydrogen lipid parameters file distributed with the program CHARMM26 (*49*). The experimental studies of SDS micelles, using X-ray scattering, give a paraffinic radius of 16.7 Å and a total radius of 22.3 Å (*50*). On the basis of the above, we have calculated the radial separation of C12 carbon from the center of micelle (origin) to be approximately 3 Å. The total radius 22.3 Å minus 1.40 Å (van der Waals radius of the oxygen at the surface of the micelles) minus 1.46 Å (oxygen−sulfur bond length) and minus 16.58 Å (S−C12 distance obtained from the SDS monomer model) gave 2.86. Assuming that the three outer oxygens bonded to the sulfur atom can in practice make an angle with the radius of the micelle giving a projection length somewhat shorter than the individual length of one O−S bond, we have rounded the distance between the center of the micelle and the C12 carbon from calculated 2.86 to 3.0 Å. The aggregation number for SDS molecules to create micelles in water is around 60 (*51*). We have adopted this value to build the model of the micelle. The 60 SDS molecules forming the micelle were placed in space around

the origin (center of the micelle) in such a way that the C12 atom of the individual SDS monomer was positioned at a distance 3.0 Å radially from the origin toward the S atom placed at 19.58 Å (3.0 + 16.58). The Cartesian coordinates of the S atoms were calculated as vertices of truncated icosahedron centered at the origin (*53*). The total radius of the all-atom model of the micelle used for further calculations were taken to be 22.44 Å (19.58 + 1.46 + 1.40) where the values in parentheses are as described above. The radius is a priori in agreement with experiments (*50*) and within ranges to that (22−23 Å) used in molecular dynamics simulations of SDS micelle in aqueous solution (*52*).

(ii) Determination of Helical Axes. To perform rotations and translations of small domains (here helices) in a uniform way in 3D space, an algorithm for calculating the helical axis from Cartesian coordinates was applied. We implemented a method of Khan as described in Christopher et al. (*54*). Without any loss of accuracy, for a perfect helix "a point on the helix" can be replaced by a C^α atom of an α-helix. In the method we used, the points on the helical axis are found by vector algebra. The angle between three consecutive C^α atoms is bisected resulting in a vector pointing toward and being perpendicular to the helix axis. Repetition of this process with a different set of C^α atoms gives another vector pointing toward and being perpendicular to the helix axis. Finally, the cross product of the two vectors perpendicular to the helix axis is perpendicular to both vectors and as such must be parallel to the helix axis. Having the direction of the helix axis and making projections of C^α atoms onto the axis one can find the radius of an α-helix and points on the helix axis (see Christopher et al. for details (*54*)). The procedure was repeated for all sets of three consecutive C^α atoms in the helix to get an average orientation of the axis vector. Projections of the first and last C^α atoms on the helix axis were used as beginning and end points respectively of an α-helix. The algorithm was implemented in XPLOR command language and can be invoked from any input files to XPLOR at any time provided the start and stop residue identifications of a helix are given. The script with code is available from the authors upon request.

(v) Hydrophobic Moment Calculations. The hydrophobic moment introduced by D. Eisenberg (*55*, *56*) is, for a known three-dimensional structure of the protein, given by

$$\mu_H = \Sigma_n H_n s_n \qquad (3)$$

Here H_n is the numerical hydrophobicity of the *n*th residue, and s_n is a unit vector in the direction from the nucleus of the α-carbon toward the geometric center of the side chain. Hydrophobicity scales are usually based on free energy of transfer between water and some organic solvent (e.g., octanol) and fraction buried (with heuristic adjustments). The two most widely used hydrophobicity scales are by Kyte and Doolittle (*57*) and Eisenberg (*58*). In the expression for the hydrophobic moment, the resulting moment can be seen as a vector sum of values for each residue projected at specified angle (∼100° for alpha helix). In our implementation, the angle between to consecutive residues was taken as an angle created by projection of lines connecting calculated centers of mass of involved residues on the plane perpendicular to the helix axis. Given the start and end points of the helix axis (see Determination of Helical Axes), the calculated hydrophobic moment vector was arbitrarily attached to the helix in the middle. Both hydrophobic scales above were incorporated as alternatives in the XPLOR script.

(d) Hydrodynamics Calculations on the Final Structures of apoCII in Complex with SDS Micelles. Hydrodynamics calculations on the final apoCII−SDS micelle complex were performed with program DIFFC by Korzhnev et al. (*59*). The orientation and size of the diffusion tensor (and the predicted Woessner τ values) as well as the orientation of the backbone N−H vectors with respect to the principal axes of the diffusion tensor were calculated. The diffusion tensor was calculated based on the backbone and side-chain atoms of apoCII and all heteronuclear atoms, except the inner C atoms 4−12, of the SDS micelle. No hydrogens were used. The atomic radii were uniformly set to 3 Å, the temperature was set to 313.1 K, and the viscosity was 6.56 10^{-4} Pa•s.

(e) Calculations of the Free Energy of Solvation of (Individual Helices) of apoCII in Complex with SDS Micelles. The method used for calculating the free energy of solvation was based on the hydropathy scale (*58*) and a *z*-dependent function (*z* perpendicular to the membrane surface) introduced originally by Milik and Skolnick (*60*). This function models the border between two phases (water/membrane) and produces a smooth transition between the various phases. We used a recent development of this method as given by Efremov et al. (*61*) and adapted their equation to our geometry of the helix on the curved (micelle) surface, where *z*-dependency has been replaced by radial dependency of the micelle. The calculations were carried out using XPLOR. To address the question of how an amphipathic helix penetrates the interface between water and the SDS micelle, we performed a number of tests using the helices of apoCII. A gradual immersing of an individual helix (with the hydrophobic moment directed into the micelle) along the radius of the micelle has been performed. A profile of the recorded solvation energy shows a somewhat dispersed well of the length of 0.6 Å around the radius of the micelle (data not shown). Taking into consideration the above findings, we adopted a sphere with a radius equal to the radius of the model of the SDS micelle to be the surface at which we placed the helical axes of the helices of apoCII. An individual helix, positioned at the surface of the model of the micelle, was rotated in steps of 10° around its (previously calculated) helix axis and the solvation contribution was recorded. The solvation contribution was referenced with respect to the situation that apoCII was not connected to the SDS micelle, by calculating for each conformation the solvation energy in the absence and presence of SDS micelles. The obtained profiles for the three helices of apoCII are analyzed in the discussion. In the script, written for the program XPLOR, we have used the equation named above with the *z*-direction replaced by the *r*-direction of the micelle and the solvent accessible surface was calculated using the algorithm implemented within XPLOR. The script with code is available from the authors upon request.

RESULTS

NMR Spectral Assignment. The ^1H, ^{15}N-HSQC spectrum of Figure 1 demonstrates the limited dispersion of the peaks of the mainly α-helical protein in complex with SDS

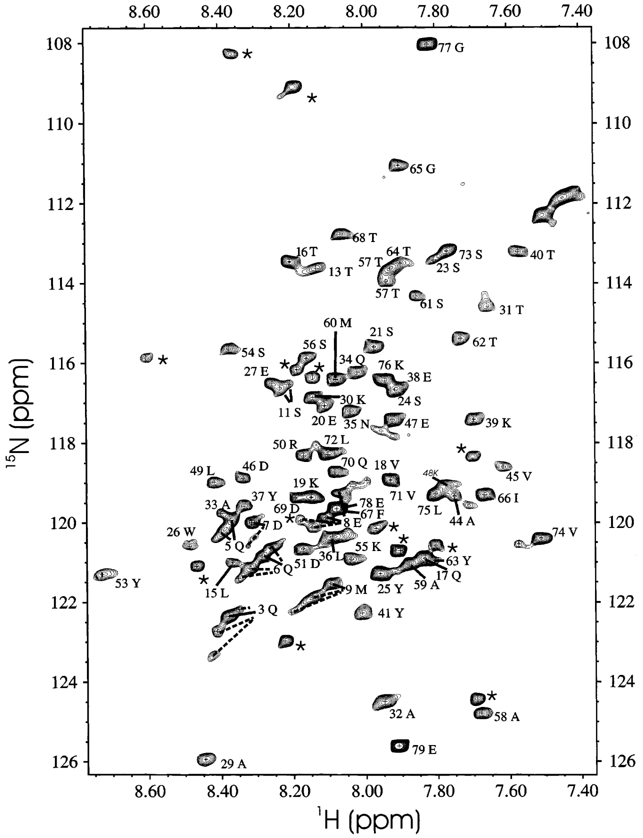

FIGURE 1: The 600 MHz ^{1}H,^{15}N-HSQC spectrum of apoCII in complex with SDS micelles. The sample conditions are as described in Materials and Methods; SDS concentration is 380 mM and the temperature is 40 °C. Labels next to the cross-peaks delineate the assignment of each resonance. The first two residues were not observed. Unassigned additional peaks were observed and were attributed to impurities or additional conformations (∗). Assigned additional minor peaks are indicated with their label (broken line).

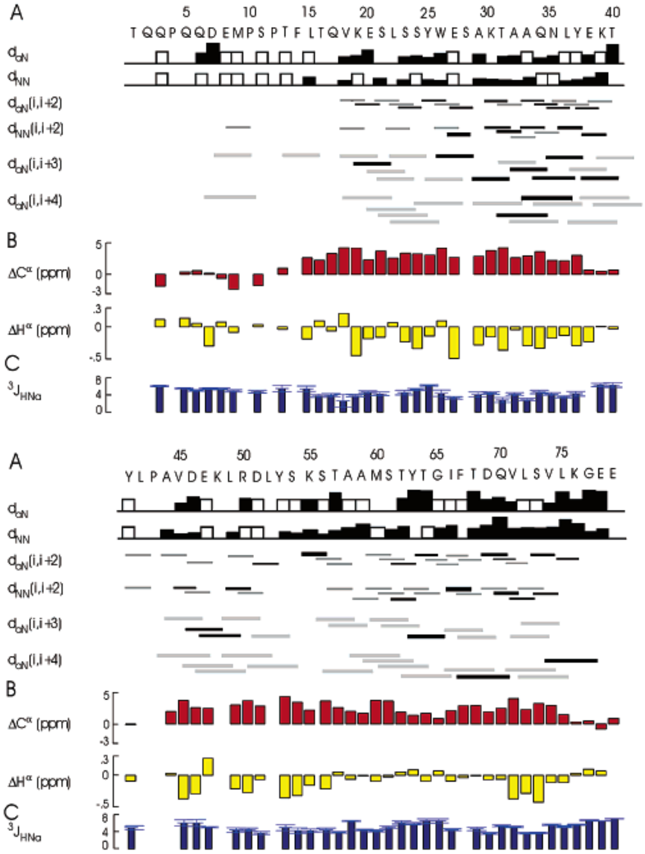

FIGURE 2: Overview of the NMR derived parameters that measure secondary structure of apoCII in complex with SDS micelles. The apoCII amino acid sequence and residue numbering is indicated in the top two lines. (A) The sequential distances characterizing secondary structure. The sequential distance from $H_{\alpha i}$ to H_{Ni+1} ($d_{\alpha N}$) and from H_{Ni} to H_{Ni+1} (d_{NN}) are shown on the first and second line of A, respectively, as open and filled bars. The height indicates the relative intensity. Filled bars indicate that for these contacts the NOE intensity could be determined reliably. For other contacts, no accurate determination of the intensity could be made due to overlap; these contacts are indicated with open bars with a single height, indicating the presence of an unambiguous contact. On the third to sixth line the other distances characterizing secondary structure are given. Black lines indicate reliable intensity determination, while gray lines indicate just the presence of an NOE contact. (B) The difference between observed and random coil shift for C$^{\alpha}$ ($\triangle C^{\alpha}$) and H$^{\alpha}$ ($\triangle H^{\alpha}$) conformational shifts (see text). (C) The $^{3}J_{HNH^{\alpha}}$-couplings (indicated as $^{3}J_{HN\alpha}$) with error margins indicated on the bars.

micelles. To overcome this resonance overlap, a double-labeled ^{13}C/^{15}N sample was employed. Thanks to additional ^{13}C labeling, it is possible to more reliably establish assignments and make them more complete than with only single labeling (^{15}N). Via standard through-bond ^{13}C/^{15}N triple-resonance experiments (Material and Methods) essentially complete backbone (^{15}N, H$_{N}$, C$_{\alpha}$, H$_{\alpha}$) and near side-chain assignments (C$_{\beta}$, H$_{\beta}$) were obtained, whereas assignment further into the side-chains was limited (BMRB entry 5534). During the course of our work, MacRaild et al. (*25*) reported backbone assignments based on a single (^{15}N) labeled sample. Our backbone assignments are more complete (residues 13 to 78, Mac Raild et al., versus residues 2 to 78 in our work, Supporting Information, Table S1). For residues 13 to 78 our assignments confirm, in as far as comparison goes, for the most part those of MacRaild et al., although some differences are observed (Supporting Information, Table S1). These differences do, however, not affect the structural conclusions.

Secondary Structure. The secondary structure of apoCII has been determined by various measures (NOEs, $^{3}J_{HNHA}$-couplings, ΔC_{α}, ΔC_{β}, and ΔH_{α}) (Figure 2). From residues 3 to 14, the data indicate a random secondary structure. For residues 15 and 16, the data are not conclusive with regard to presence of α-helix. From residues 17 to 38, an α-helix is present (helix 1). From residues 39 to 44, the α-helix is disrupted. From residue 45 onward to residue 74/75, the secondary structure is α-helical. For residues 61 to 65, the helix propensity is somewhat decreased. The α-helix NOE patterns are still present, the ΔC_{α} and ΔH_{α} are smaller but still compatible with a α-helical conformation. The $^{3}J_{HNHA}$-couplings are increased above 6 Hz. Also, for residues 58 and 59 a reduction in ΔC_{α} and ΔH_{α} is seen, while only A58 shows a higher $^{3}J_{HNHA}$-coupling. We therefore designate the region from residue 45 to residue 57 as helix 2 and the region from residue 65 to 74/75, which is essential for activation of LPL, as helix 3. From residue 76 on to the last residue 79 the chain is in a random coil state. These secondary structure designations are similar to those found by MacRaild et al. (*25*).

Relaxation Measurements. Relaxation measurements of T$_{1}$, T$_{2}$, and NOE for the ^{15}N spins of the backbone were carried out at ^{1}H frequencies of 400 and 600 MHz (Figure 3, Table S2). The T$_{1}$ and T$_{2}$ at the two different fields display a

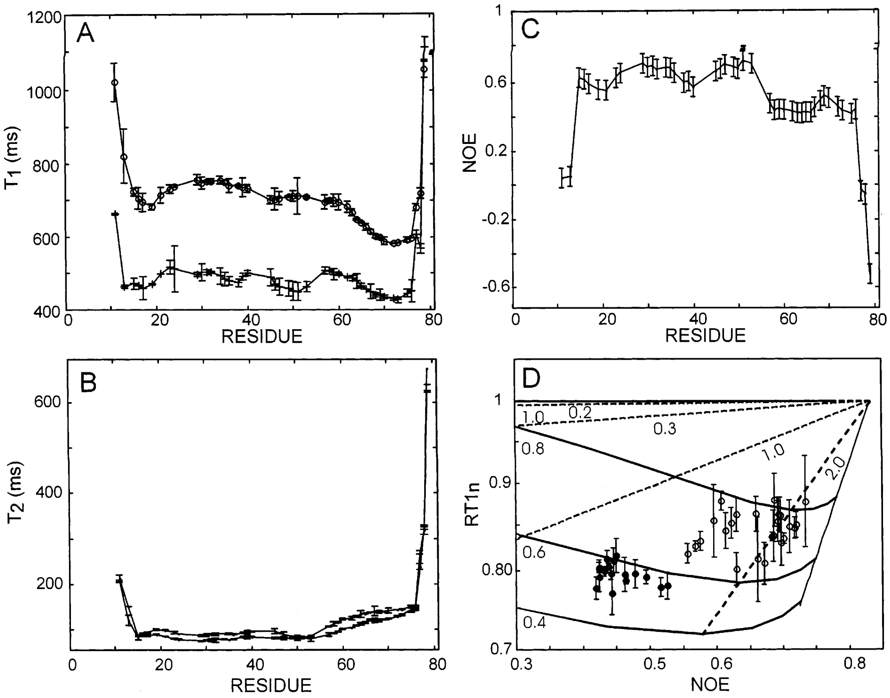

FIGURE 3: Relaxation data T_1 (A), T_2 (B), and (^{15}N, ^{1}H) NOE (C) of the ^{15}N nuclear spin of the backbone of apoCII in complex with SDS micelle at 40 °C and measured at 400 and 600 MHz ^{1}H frequency. Due to overlap a number of resonances could not reliably be integrated and were excluded form the analysis. To show trends, the T_1, T_2, and NOE data were smoothened via a three-point window. (D) RT1n versus (^{15}N, ^{1}H) NOE at 600 MHz showing the presence of nanosecond time scale internal motion (ns-im). When RT1n equals 1 only picosecond internal motion (ps-im) is present. RT1n < 1 shows the presence of ns-im. RT1n is RT1 ($= T_1\_600/T_1\_400$) corrected for the linear dependence on NOE due ps-im (see text) and normalized by 1.82. This value corresponds to RT1 in the absence of internal motion for a molecule with an overall tumbling time τ_m° of 11.0 ns. The labeled drawn contour lines correspond to the RT1n values when the squared-order-parameter S^2 is 0.4, 0.6, 0.8, and 1.0, respectively (labels at left from bottom to top). The labeled straight broken lines correspond to RT1n values when the time constant for internal motion τ_i equals 0.2, 0.3, 1.0, and 2.0 ns. The RT1n values of residues in helix 3 are indicated with filled circles. The lower RT1n shows that these residues have a higher degree (lower S^2) of ns-im. A complete overview of all relaxation parameters is given in the Supporting Information (Table S2−S4 and Figures S1−S3), while Table 2 gives a summary of the final average results per helix.

sequence dependence that is markedly similar. Figure 3A shows that the T_1 data at the two fields are essentially constant throughout helix 1 and helix 2. For the N- (1−14) and C-terminal residues (76−78), the T_1 values are higher as expected for random coil region with increased internal motion. Most interestingly, from approximately residue 60 to residue 70, T_1 decreases to the lower level of helix 3, indicating different internal motion characteristics for helix 3. The T_2 data in Figure 3B shows a similar trend. For helix 1, T_2 is essentially constant and then gently slopes up from approximately residue 53 (toward end of helix 2) onward to residue 75. The transition seen in the T_1 data between residues 60 and 70 is faintly visible also in the T_2 data. Near either end of the molecule the T_2 data dramatically increases, showing again increased internal motion of the N-terminal and C-terminal residues. The latter is also evident from the negative or near negative NOEs observed for the N- and C-termini (Figure 3C). The residues of helix 1 and helix 2 have relatively low NOE values (0.6 to 0.7), indicating a limited but higher degree of internal motion than found in the inner core of well-defined proteins. Interestingly, the NOE drops between residues 53 to 58 and is at the lower level of helix 3 (NOE 0.4 to 0.6) up to residue 75, indicating again the different internal mobility of helix 3. In summary, the relaxation data show that the activation helix (helix 3) has different internal motion characteristics than helix 1 and 2.

Dynamics of the Backbone. We have analyzed the relaxation data using new software and extracted the motional parameters (see Materials and Methods). In the usual analysis, it has to be assumed that the time scale for internal motion is fast (picoseconds, $\tau_i < 200$ ps, ps-im). This analysis fails when many residues undergo nanosecond time scale internal motion (ns-im), as is the case here. By employing our analysis method on relaxation data measured at two fields (*43*), it was possible to extract the residue-specific overall-tumbling time (τ_m°) and to establish the degree (squared order parameter S^2) and time scale(s) of internal motion (τ_i), even in the presence of ns-im.

A qualitative analysis of the normalized RT1n ($= T_1\_600/T_1\_400$) versus NOE (Figure 3D) shows the presence or absence of ns-im as reduction of RT1n. Two important conclusions can be drawn. All helix residues experience ns-im, because they have RT1n < 1. Second, the RT1n values for helix 3 are smaller (0.80 ± 0.04) than for helix 1 and helix 2 (0.83 ± 0.04), showing that helix 3 experiences a larger contribution of ns-im. The results of the full analysis are given in Figure 4 and Supporting Information (Tables S2−S4 and Figures S1−S2). Most notable is that helix 3 has a larger degree of ns-im (Figure 4), while the degree of ps-im is similar for the three helices. A summary of the results, characteristic for the three helical regions, is presented in Table 2.

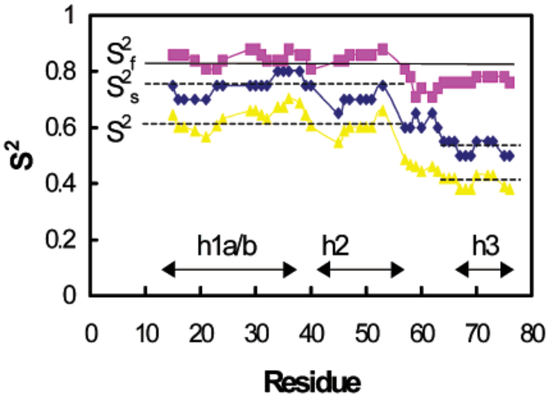

FIGURE 4: Squared order parameters of the internal motion of the ^{15}N backbone of apoCII in the apoCII−SDS micelle complex at 40 °C, showing the increased internal motion of helix 3 on the nano second time scale. S^2_f is the squared order parameter of the fast (picosecond) internal motion, S^2_s is the squared order parameter of the slow (nanosecond) internal motion, while S^2 is the total squared order parameter ($S^2 = S^2_f S^2_s$). The time scales for internal motion are given in Supporting Information (Figure S1).

Table 2: Structural Characteristics of the ApoCII−SDS Micelle Complex

	overall	helix1/helix 2	helix 3
residue	1−79	16−38/45−57	65−74
R_1 (s^{-1})		1.38(5)	1.62(12)
R_2 (s^{-1})		12(1)	8.1(9)
(^1H, ^{15}N) NOE		0.70(7)	0.43(7)
$S^2(R_2)$		0.60	0.43
S^2_s		0.70	0.55
τ_{is} (ns)		2.0	2.0
S^2_f		0.84	0.78
τ_{if} (ns)		0.02	0.04
τ°_{m} (ns)	11.2	12.0(0.6)	9.5(0.4)
$\tau^{\circ,max}_{m}$	13.5		
$\tau^{\circ,min}_{m}$	8.7		
$D_{\|\|}D_{\perp}$	2.2		
Φ (°)		25	55

The τ°_{m} derived after correction for the time scale of internal motion (Materials and Methods and Supporting Information, Table S2, Fig. S2/3) shows that helix 1 and helix 2 have about the same τ°_{m} of 12.0 ± 0.6 ns, while helix 3 has a lower τ°_{m} of 9.5 ± 0.4 ns (Table 2). The distribution of τ°_{m} (Figure S2/3) reports on the size and shape of the diffusion tensor (Materials and Methods). Excluding the C- and N-terminal residues as unreliable, we find that $\tau^{\circ,max}_{m} \approx 13.5$ ns and $\tau^{\circ,min}_{m} \approx 8.7$ ns. From these values, it can be derived that the anisotropy $D_{||}D_{\perp}$ is ca. 2.2 (Materials and Methods, eq 2), which is consistent with a molecular complex consisting of a micelle and an apoCII molecule on and extending from its surface. The orientation of each N−H bond with respect to the long axis of the diffusion tensor could then be derived from the relaxation data (Materials and Methods, eq 1). Since the N−H vectors in a helix point approximately along the helix axis, their average value per helix is a good measure for the helix axis orientation. We found that helix 1 and helix 2 are close to parallel to the main axis of the molecular diffusion tensor (angle ≈ 25°). Helix 3 is oriented closer to perpendicular with an angle of ca. 55° (Table 2).

Structure Calculations Based on Classical NMR Constraints. Starting from an extended helical structure, 100 structures were calculated via a standard simulated annealing (SA) protocol and using the classical NMR constraints (Table 3). We obtained relaxed, low energy structures with good convergence; the energy-sorted structures showed a plateau up to structure 96; only the last 4 had a slightly elevated NOE energy. The satisfaction of dihedral constraints and J-coupling constants was almost perfect, and no NOE distance violations were larger than 0.3 Å (Table 3).

Table 3: Statistics over the Accepted Structures Using "Classical" NMR Constraints[a]

NMR-derived constraints	
intraresidue distances	
interresidue distances	236
dihedral angles	104
$^3J_{HNH\alpha}$ couplings	56
NMR relaxation constraints on orientations of helices helix 1/helix 2/helix 3	not used
constraints violations	
rmsd for bonds	0.0022 Å (maximum < 0.01 Å)
rmsd for angles	0.54° (maximum < 1°)
NOE distance violations	none > 0.3 Å
dihedral angle violations	none > 5°
energies of structures	
bond	6.13 ± 0.24 kcal/mol
angle	98.92 ± 1.57 kcal/mol
improper	18.01 ± 0.31 kcal/mol
van der Waals	2.07 ± 0.53 kcal/mol
constraints on dihedrals (backbone)	0.07 ± 0.02 kcal/mol
NOE	28.72 ± 1.21 kcal/mol
J-couplings	0.01 ± 0.00 kcal/mol
total	153.93 ± 3.46 kcal/mol
rmsd comparison of backbone atoms	
helix 1 [residues 16−38]	0.96 ± 0.43 Å
helix 2 [residues 45−58]	0.64 ± 0.21 Å
helix 3 [residues 64−74]	0.08 ± 0.07 Å
residues 16−74	8.62 ± 2.87 Å

[a] Averages and standard deviations of energies, constraint violations, and RMSDs calculated for 96 structures. Pairwise RMSD calculated compared to the structure with the lowest energy.

Superpositions of the calculated 100 structures show that the three helices of apoCII are each well defined (Table 3). Helix 1 is somewhat flexibly kinked around residues 26−29, giving it overall a concave appearance, although some structures are straight and some are even slightly convex (Figure 5, top right). As a consequence, superposition of the first and second half of helix 1 leads to smaller rmsd values (0. 42 and 0.11 Å) than for the whole helix 1 (0.96 Å) (Table 3). A similar observation was made by MacRaild et al. (*25*).

A second interesting feature is that helix 2 and 3 retain a relatively straight conformation. Helix 3 bends away from helix 2 uniformly in different directions over an angle of no more than ca. 20° (Figure 5, top left and bottom left, spread of blue structure). This limited flexibility is because the junction region between these two helices (residue 59−63) is helical. Again similar features have been observed by MacRaild et al. (*25*).

The most salient aspect of the structure set is the lack of definition in the relative orientation of helix 1 with respect to helix 2 and 3 (Figure 5, all views). Although one can observe some "statistically" preferred directions, they cover almost uniformly the "northern" semisphere of the 3D space. It should be noted that the junction region 39−44 is not completely flexible. Closer examination of the structures

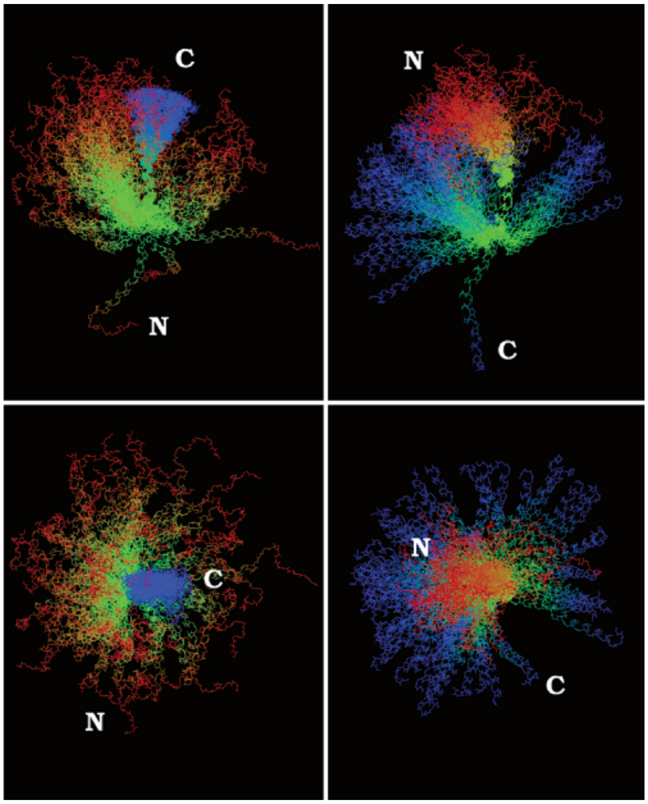

FIGURE 5: The backbone atoms of the 96 accepted structures of apoCII calculated using "classical" NMR constraints (NOE distances, dihedral constraints, and *J*-coupling constants). Right top and bottom: residues 29−38 (helix 1b) in RMSD comparison. Right bottom is a 90° rotation of right top view around the horizontal axis. Left top and bottom: residues 45−58 (helix 2) in RMSD comparison. Left bottom is a 90° rotation of left top view around the horizontal axis. 95 structures are superimposed on the structure with the lowest energy. The continuous color change for this and all following structure figures: red is N-terminus and blue is C-terminus.

shows that the flexibility of the junction essentially originates from rotations around the bonds between residues 42 and 43.

In conclusion, analysis of the apoCII structures shown in Figure 5 showed that classical NMR constraints alone are not sufficient to produce a well-defined overall 3D conformation of the molecule. Additional constraints are required.

Global Structure of apoCII and SDS Micelle. To derive the global 3D structure of apoCII in complex with SDS micelles, we implemented an algorithm that refines the structures derived via classical NMR constraints by adding three classes of global constraints.

(i) The orientations of helices derived from NMR relaxation measurements at two fields (Table 2).

(ii) The constraints derived from the fact that the apoCII molecule is attached to the SDS micelle surface, as all helices show NOE contacts with the SDS micelle (*25*). To create a surface on which we could perform our orientations of the helices, we built an accurate all-atom model of the SDS micelle. The total radius of the calculated SDS micelle was 22.44 Å, in agreement both with the radius obtained by experimental studies (22.3 Å, (*50*)) and the radius (22−23 Å) used in the molecular dynamics simulations of SDS micelles in aqueous solution (*52*).

(iii) The constraints derived from the hydrophobic interaction with the SDS micelle. To steer the orientation of the hydrophobic faces of the amphipathic helices of apoCII, we have implemented the hydrophobic moment as introduced by Eisenberg (*55*, *56*).

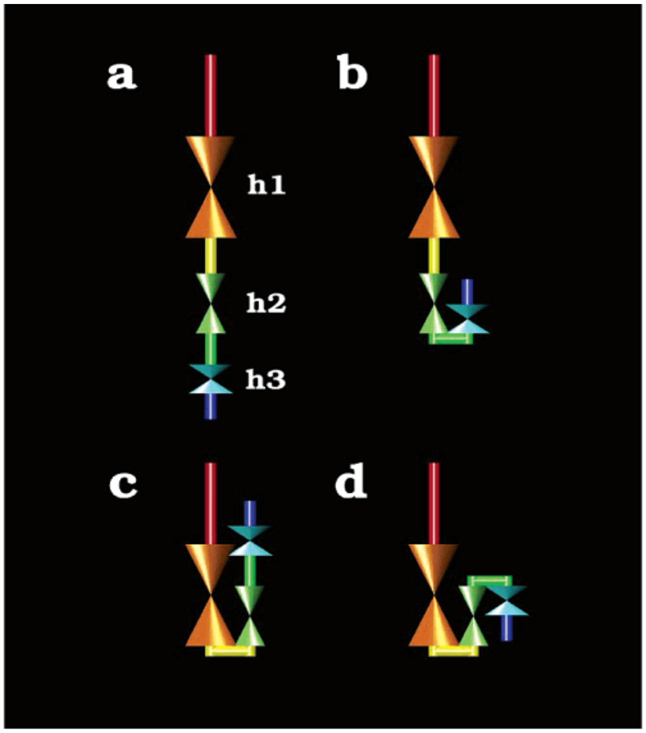

FIGURE 6: Four cases representing the solutions consistent with the helix orientations derived from NMR relaxation data. Each helix is displayed as a double-headed cone, to account for the directional degeneracy of the NMR-derived orientations (Table 2). The three helices of apoCII: helix 1 (h1) residues 16−38; helix 2 (h2) residues 45−58; helix 3 (h3) residues 64−74. The helical axes stay on the cones defined by their respective orientations with respect to the symmetry axis of the diffusion tensor. The direction of the first helix (h1) was treated as nondegenerate without loss of generality. Cases a, b, and d are rejected, and case c is accepted and submitted to further calculations (see text).

Prior to application of the global refinement protocol, we qualitatively assessed the conformational space that would be available after application of the global restraints derived from NMR relaxation data, i.e., the orientations of helices (global restraint class 1). Helix orientations derived from NMR relaxation measurements are degenerate. Each helical axis is confined to a cone with a half-angle defined by the orientation angle obtained from the NMR relaxation experiment. In addition, each helix axis can satisfy the angle by pointing up or down. Taking this into consideration, and the fact that the orientation of the first helix does not need to be permuted in space without loss of generality, four cases had to be considered (Figure 6). Case a (all helices more or less in one line) can be discarded immediately, because in such a conformation the molecule would be too long to fit on the surface of the micelle. Cases b and d can be discarded, because they require a deviation larger than 90° for the orientation of helix 3 with respect to helix 2. Such a large deviation was not observed in the structures using classical NMR restraints (Figure 5, top left). This leaves case c (helix 1 and helix 2 make a sharp angle; helix 2 and helix 3 more or less in line) as the only conformation consistent with the helix angles derived from the NMR relaxation data.

The 100 structures calculated using classical NMR constraints were submitted to the final orientation/facing/

Table 4: Statistics over the Accepted, Final Structures Using "Classical" and "Global" NMR Constraints[a]

NMR-derived constraints	
intraresidue distances	
interresidue distances	as before
dihedral angles	as before
$^3J_{HNH\alpha}$ couplings	as before
NMR relaxation constraints on orientations of helices helix 1/helix 2/helix 3	25°/25°/55°
constraints violations	
rmsd for bonds	0.0029 Å (maximum < 0.01 Å)
rmsd for angles	0.59° (maximum < 1°)
NOE distance violations	none > 0.4 Å
dihedral angle violations	none > 5°
energies of structures	
bond	10.68 ± 1.46 kcal/mol
angle	120.67 ± 8.66 kcal/mol
improper	24.14 ± 2.20 kcal/mol
van der Waals	8.90 ± 3.58 kcal/mol
constraints on dihedrals (backbone)	0.23 ± 0.12 kcal/mol
NOE	53.81 ± 9.34 kcal/mol
J-couplings	2.93 ± 0.07 kcal/mol
total	221.36 ± 22.31 kcal/mol
RMSD comparison of backbone atoms	
helix 1 [residues 16−38]	0.39 ± 0.15 Å
helix 2 [residues 45−58]	0.67 ± 0.23 Å
helix 3 [residues 64−74]	0.24 ± 0.11 Å
residues 16−74	0.85 ± 0.24 Å

[a] Averages and standard deviations of energies, constraints violations, and RMSDs calculated for 68 refined, accepted structures. Pairwise RMSD calculated compared to the structure with the lowest energy.

refinement protocol. Of these 100 structures, 68 passed an acceptance test for ranges of bonds, angles, distance constraints, and dihedral restraints. Their structural characteristics are shown in Table 4. Because helix 1 is bent to fit the surface of the micelle, it was treated operationally as two separate helices h1a and h1b (Figure 5, top right) both with the orientation angle 25° but on different "cones". Among the 68 accepted structures, there are no structures with NOE distance violations greater than 0.4 Å and dihedral angle violations greater than 5°. For the 15 structures with the lowest total energy, there are no NOE distance violations greater than 0.3 Å. The covalent structure of apoCII is also well preserved. Only a slightly higher rmsd is observed for violations of bonds and angles, compared to the corresponding values for the initial calculations (compare Tables 3 and 4, 0.0029 against 0.0022 for bonds and 0.59° against 0.54°). The partial energy terms all show uniformly higher but comparable energies. The NOE energy is now ∼54 kcal/mol compared to ∼29 kcal/mol for the initial calculation. One has to keep in mind that in the final calculation we had to satisfy additional constraints imposed on the system, so an increase of the total energy is not unexpected.

The rmsd for the complete molecule (residues 16−74) is below 1 Å (Table 4) thanks to the application of the global constraints. This is an enormous reduction from the rmsd of 8 Å (Table 3) obtained when using only classical NMR constraints. Thus, we have been able to define the 3D spatial arrangements of the three helices of apoCII on the SDS micelle. The rmsd comparisons of backbone atoms for the three helical regions in apoCII show some interesting features compared to the initial calculation. The rmsd for helix 1 (residues 16−38) went down significantly, from 0.96 Å in the initial calculation to 0.39 Å in the final calculations, indicating an elimination of the less-well-defined regions along the sequence (compare Tables 3 and 4). The rmsd for helix 2 (residues 45−58) and helix 3 (residues 64−74) stay comparable in both calculations, ensuring that nothing dramatic happened by imposing the additional constraints in terms of orienting and facing the helices during the process of refinement (compare Tables 3 and 4).

The final globally defined structures of apoCII on the SDS micelle are shown in Figure 7 in three different views. They are superimposed by orienting and facing the helices and positioned on the transparent sphere representing the SDS micelle. As can be seen, the global structure is now well defined, except for the N-terminal part consisting of residues 1 to 15. From the all-atom presentation (Figure 7, left), it can be estimated that the complex has dimensions of ca. 38 by 48 by 74 Å. To further validate the correctness of the global fold, hydrodynamic calculations were performed on a representative member of the set of final structures (see also Supporting Information Figure S3). This gave a maximum τ_m° of 13.8 ns (Fig. S3, legend), a value close to the experimental maximum τ_m° of 13.5 ns (Table 2). Back calculation of τ_m° for each N−H vector shows good correlation with the experimental τ_m°, and is optimal when the maximum τ_m° is set to 13.5 ns and $D_\parallel/D_\perp$ is 1.8 to 2.0 (Figure S3). The asymmetry of the complex $D_\parallel/D_\perp$ is calculated to be 1.56 (Fig. S3), which is smaller than the $D_\parallel/D_\perp$ value of 2.2 estimated from the τ_m° distribution (Table 2) and the value of 1.8 derived from the back calculation. A somewhat more extended random coil region (residues 1−16) can easily increase this ratio.

From the frontal view in Figure 7 (middle), it can be appreciated that the average hydrophobic moments of the helices point to the center of the SDS micelle. Going from the N-terminus to the C-terminus it can be seen that helix 1 (parts a and b) lies on the SDS surface. The backbone makes a near 180-degree turn between residues 39 and 43 so that helix 2 and helix 3 run upward again over the micelle surface. In the structure, no close side-chain contacts are evident between helix 1 and helix 2 or 3. In accordance with this, MacRaild et al. (*25*) did not report evident long-range NOE contacts, and neither did we find evidence for readily assigned NOE contacts, such as between methyl protons and backbone protons. However, it should be noted that the absence of long-range NOEs is practically impossible to prove due to resonance overlap even when employing doubly labeled protein. Note that between helices 2 and 3, the helical character of the backbone is hardly disrupted in accordance with experimental observations (classical NMR constraints, Figure 2). However, as can be seen in Figure 7 (right) there is a slight bend after helix 2 (in the region between residues 58−63), so that helix 3 nicely attaches itself to the surface. Note that because helix 2 makes an angle of ca. 25° with the main axis of the diffusion tensor and helix 3 of ca. 50°, the angle between helix 2 and helix 3 is relatively small. In other words, the structure fits both the classical NMR constraints, which define the secondary structure, and the global constraints from, for example, relaxation data, which define the helix orientations. The hydrophobic side-chains (white in Figure 7, right) all point toward the micelle interior in helices 1 and 2. For helix 3 the distribution of hydrophobic side chains is different. Although the average hydrophobic

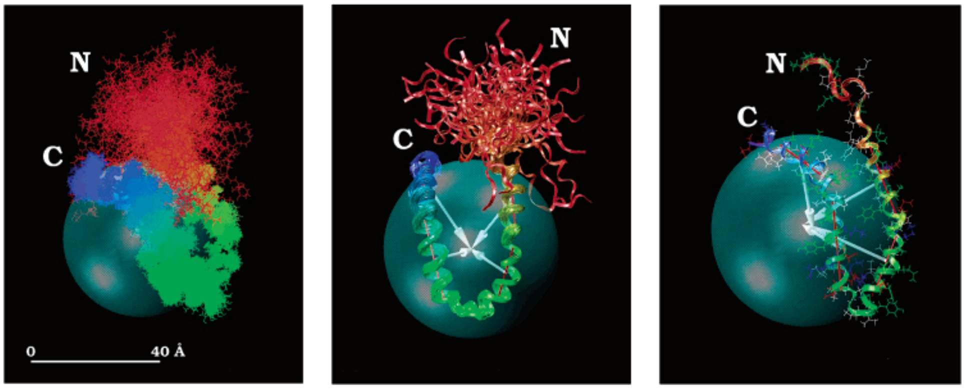

FIGURE 7: Different views of apoCII in complex with an SDS micelle after the final global refinement protocol (see text). Left panel: Superposition of the final set of 68 accepted structures of apoCII (all-atoms in "lines" style) shown in complex with a transparent surface of the size of an SDS micelle of radius 22.5 Å. Middle panel: The final set of 68 accepted apoCII structures in ribbons representation. The red thin cylinders depict the calculated helical axes of the structures (shown for 1 structure). The white arrows represent the calculated hydrophobic moments of the three helices of apoCII shown with a length uniformly set to the radius of the SDS micelle. Right panel: Lowest-energy structure of apoCII of the final set of 68 accepted structures. The structure is presented as lines and ribbons. The red thin cylinders show the helical axes and the white arrows represent the directions of the calculated hydrophobic moments pointing into the micelle. The length of the arrows is set to be equal the radius of the micelle.

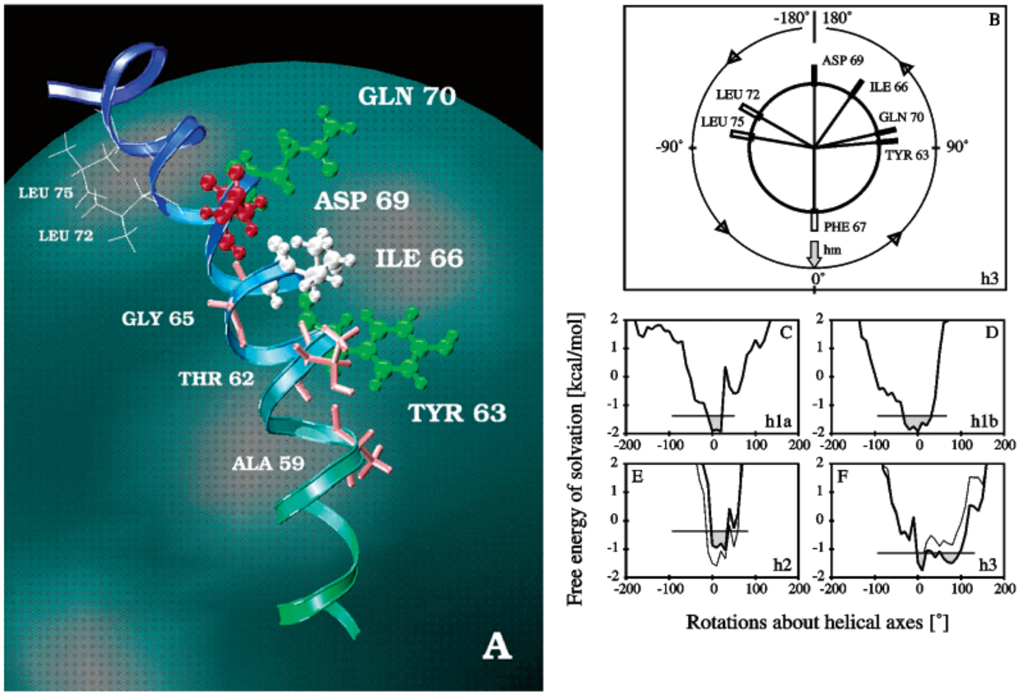

FIGURE 8: Analyses of helix 3 with regard to hydrophobic residues and hydrophobic free energies. (A) Detailed view of helix 3 showing the arrangement of hydrophobic and conserved residues. The residues that appear most crucial for activation of LPL (*20*) are shown by a ball-and-stick representation. The additional three that are conserved, but less crucial (*20*), are shown as pink sticks. White labels represent hydrophobic residues. (B) Schematic of helix 3 viewed along the helix axis from residues 64 toward 75. The fully conserved residues are shown as small black-filled rods and other hydrophobic residues as open rods. The hydrophobic moment of helix 3 (hm) is at an angle of 0° as in the final structures and points toward the center of the micelle. (C−F) Hydrophobic interaction energies calculated as described in Materials and Methods as a function of the rotation angle about the helix axes. The hydrophobic interaction energy is calculated as the difference between apoCII bound and not bound to the SDS micelle. The same conformation of apoCII is used (one of the set of 68 final structures), so that the calculated value truly reflects hydrophobic interaction energy. The gray area, running in each panel up to ca. 1 kT from the minimum, indicates the energetically (hydrophobic) allowed region. Note that the minimum in hydrophobic energy nicely coincides with the orientation of the hydrophobic moment in the final structure. The helices are defined as described in the text, namely, helix 1a (16−26), helix 1b (29−38), helix 2 (45−58), and helix 3 (64−74). The thin lines in E and F represent the results obtained when residue A59 or L75, respectively, was also included in the free energy calculation.

moment points to the micelle interior, a number of the hydrophobic residues point away from the interior. Residue 66 is pointing out from the micelle toward the solution. This less-well oriented distribution of hydrophobic residues has consequences for the definition of the orientation of the hydrophobic moment of helix 3 and may provide insight into the mechanism of activation (see below in Discussion and Figure 8).

DISCUSSION

We have determined the global 3D structure and dynamics of apoCII in complex with SDS micelles. MacRaild et al.

determined the apoCII structure in complex with SDS micelles by using classical short-range NMR restraints derived from a single (^{15}N) labeled apoCII sample. The present study extends the work of MacRaild and co-workers (*25*) by using double (^{15}N/^{13}C) instead of single (^{15}N) labeled apoCII and most importantly by defining the global structure of apoCII in complex with SDS micelles and by exploring the dynamics of apoCII in the complex. The secondary structure we found is essentially the same as that found by MacRaild et al., but the additional ^{13}C labeling provides more reliable definition. When employing only classical short-range NMR restraints, we observe, as MacRaild et al. did, a lack of global definition. However, application of three types of global restraints allowed us to define the global 3D structure of the apoCII−SDS micelle complex. SDS is now commonly used in NMR studies of lipid-binding proteins (*9*−*11*, *13*, *23*, *25*, *27*, *62*) and has been shown to be a good mimic of phospholipid surfaces (*27*). It seems therefore valid that many of the structural conclusions using SDS micelles can be generalized to lipoproteins. Together with previous mutagenesis studies, the present studies provide new information about the mechanism whereby apoCII serves as a physiological activator of lipoprotein lipase.

Arrangement of Amphipathic α-Helices and Hinge Regions. One way of viewing apoCII in the complex with SDS (Figure 7) is that it consists of two long helices. The first helix (helix 1a/b) runs from residues 16−38 and the second one, consisting of helix 2 and 3, runs from residues 45 to 74. These two helices seem flexibly linked because the overall 3D structure of apoCII seen in the complex stems from the interaction of these helices with the micelle surface (compare Figure 5 with Figure 7). These overall features of the apoCII structure are remarkably similar to those of other exchangeable apolipoproteins for which structural data are available, e.g., apoE, AI, and LpIII (5). All consist of extended helices connected via flexible hinge regions. In LpIII the structure has been determined in the absence of lipid, i.e., in a water environment. Under these conditions, the molecule folds into a five-helix bundle. In this bundle, the hydrophobic residues are hidden from water in the interior. It has been suggested that upon lipid binding the helices of the bundle spread out, so that they attach their hydrophobic faces to the lipid (5). In the case of apoCII, we directly observe the end result of this process, namely, the attachment of the helices to the SDS micelle surface. The hinge region (39−44) may allow apoCII to spread out over larger particles, e.g., VLDL or chylomicrons, leading to a more extended conformation than depicted in Figure 7.

Amphipathic helices in apolipoproteins are generally about 11 or 22 residues in length corresponding to 3 or 6 complete turns of the helix (2). This length probably satisfies both the requirements for sufficient hydrophobicity and for sufficient flexibility. If the amphipathic helix is longer there will be a certain twist between the polar and nonpolar faces of the helical rod, which may be disadvantageous for its interaction with lipids (*2*). In the apoCII−SDS micelle complex such a twist is observed in helix 1 (16−38). The hydrophobic surfaces of helix 1a and 1b are slightly twisted relative to each other. To bind to the micelle surface, helix 1 has to weakly bend around residue 27, leading to helices 1a and 1b. Each helix is again ca. 11 residues long. After the hinge region (39−44), helix 2 (45−58) forms one rigid rod, followed by the transition region, and helix 3 from residues 64 to 74. Thus, another view of apoCII is to consider it as consisting of four helices, each ca. 11 residues long. Helices 1a and 1b are connected via a weakly flexible helical hinge, helix 1b and helix 2 are connected via a flexible hinge, and helix 2 and helix 3 are connected via a longer helical hinge region. The helical hinge regions allow for only limited flexibility (see Figure 5).

For apolipoproteins secondary structure programs predict the structure generally quite well. This becomes also evident from the present study on apoCII. The differences between previous predictions and current observations are that helix 1 is predicted as one long helix, instead of the observed weak helix kink between residues 26−29. Second, the region from 56 to 67 is predicted to be a coil, whereas experimentally a flexible, but helical, hinge region is observed. ApoCII sequences from different animal species show on average ca. 30 to 35% sequence identity, in comparison between mammalian sequences (very conserved) and other vertebrates (chicken and fish) (*18*, *19*). The predicted secondary structures are however generally similar to those for human apoCII. Interestingly, for the most dissimilar sequence, the one from trout apoCII, the secondary structure for region 16−38 is predicted to consist of two helices (from 15 to 24 and from 31 to 39) connected by a coil region (Shen et al., unpublished). These helical regions are essentially identical to helices 1a and 1b. This corroborates the conclusion that short (11 residues) amphipathic helices are optimal for productive binding to the lipoprotein particles.

Internal Dynamics of apoCII. On the basis of the sequence properties Segrest distinguishes class A amphipathic helices, which have a well-defined orientation of the hydrophobic face and class G* helices, which have a less well-defined hydrophobic face (*2*). According to these definitions, helix 1a/b and helix 2 belong to class A, while helix 3 belongs to class G*. The analyses of the dynamics of the backbone of apoCII in the apoCII−SDS complex show that the class A helices, helix1a/b and helix 2, have indeed similar dynamic properties. They are characterized by a squared order parameter for ps-im ($<$ 200 ps) of ca. 0.8 (Figure 4). This high degree of order is in accordance with the secondary structure parameters, which point to well-defined α-helices (Figure 2). The most interesting observation we have made is that in addition to the ps-im, these helices undergo ns-im (1.5 to 2.5 ns) with a squared order parameter of 0.7 (Figure 4). The time scale suggests that the latter type of internal motion can be attributed to domain motion, that is, motion of the complete helix. This could for example be a rolling motion of the complete helix. The squared order parameter of 0.7 corresponds to a wobbling motion over ca. 18° (*63*). The class G* helix, helix 3, has approximately the same degree of ps-im as the class A helices. In other words, its secondary structure remains well defined with no apparent change in the degree of local dynamics. However, it shows an increased degree of ns-im motion (squared order parameter 0.55, corresponding to a wobbling motion of ca. 27°).

The Transition Region between Helix 2 and Helix 3. The data of Storjohann et al. (*23*) on an apoCII fragment spanning both helices 2 and 3 indicate that there are two α-helices in this region, interrupted by a random region spanning residues 59−66. We also find a transition region between helices 2 and 3, roughly running from residues 58−64, as evident from the relaxation data (see, e.g., Figure 3, Figure 4, and Figure S3). However, the relaxation studies show no apparent increased dynamics in ps-im for this region. The reduction in secondary shifts and increase in J-coupling values (Figure 2) is therefore likely related to a less perfect α-helical conformation, which is needed to accommodate the bend angle of ca. 30° of helix 3 relative to helix 2 (Table 2 and Figure 7). The NMR data show that this bend angle is likely induced by the necessity of attachment to the micelle, because in the absence of global NMR constraints helix 3 can bend with respect to helix 2 by ca. 30° (Figure 5 versus Figure 7).

Properties of the Hinge Region 39−44. The hinge region between residues 39 and 44 connect helix 2 and helix 3. The change in N−H vector orientation due to the hinge is evident in the change in τ values and is well reproduced in the final structures as evidenced by the back-calculated τ values (Figure S3). That the hinge region is potentially flexible is evident from the variation in helix orientations when no global constraints are applied; the flexibility is located between residues 42 and 43 (Results, Figure 5). In the complex, the residues of the hinge region do not show increased flexibility relative to residues within the surrounding helices (Figure 4). This is not surprising if one realizes that the hinge region is short and contains or is surrounded by a number of hydrophobic residues, which can interact with and anchor to the SDS micelle.

In the structures of the exchangeable lipoproteins apoE and LpIII one sees in the absence of lipids a helix bundle structure, which opens up via the flexible region when it attaches to the lipid surface (*5*). The hinge regions contain hydrophobic residues that can interact with the lipid. It is thought that these hydrophobic hinge residues provide the initial anchoring to the lipid particle. A similar mechanism may be at play in the initial phase of binding of apoCII to lipids, because the hinge region of apoCII also contains hydrophobic residues. We note however that L42 and P43 are hydrophobic residues, which point in our model toward the solution (Figure 7, right). It is conceivable that these residues may transiently anchor to another lipid particle and thereby be involved in the transfer of apoCII between lipid particles. It is not known whether the transfer goes through a water-soluble state, but since apoCII can only form a two-helix bundle, it is expected to have a lower solubility than the four- and five-helix bundle proteins apoE and LpIII. This mechanism may then form an alternate route for the exchange of apoCII between lipid particles.

In the human sequence, the break in helix conformation occurs at the single Pro residue in the hinge region at position 43. Most other apoCII species have one Pro residue in the hinge region, namely, at position 43 or 42. In chicken apoCII, there are even three Pro residues in this region (Pro42, Pro43, and Pro46). Rat and trout apoCII form exceptions in that they have no Pro residues in this region. Nevertheless, rat apoCII is very similar to human apoCII in this region (only P43T and A44S). As in human apoCII, a coil region is predicted by secondary structure programs. Since the predicted secondary structure for rat apoCII is similar to that for human apoCII, the Pro residue is probably not the only explanation for the break in the helical structure at this point (Shen et al., unpublished).

Domain Motion of Helix 3 Compared to Helix 1 and 2. The LPL activation region of apoCII has previously been narrowed down to helix 3 (*15*). According to our results, helix 3 is differs from helices 1 and 2 by its larger degree of domain motion. We therefore investigated more closely the nature of this motion. Generally, any rotational motion can be described by three Euler angles defined relative to a local axes system. In the case of helix 3, this motion can be decomposed as follows: a motion off the surface of the micelle, a motion over the surface of the micelle, and finally a rolling motion of helix 3 around its helix axis. The question to be answered is which of these or which combinations of these motions actually occur. We carried out careful hydrophobic energy calculations (Materials and Methods) to determine the effect on the free energy of certain of these motions, the results of which are shown in Figure 8.

Figure 8A shows the four most important conserved residues for activation as well as the three hydrophobic residues that are functionally conserved. The latter are presented in a more schematic fashion in Figure 8B, while Figure 8C−E shows free energies calculated as function of the rotation of each helix around its axis. The hydrophobic free energy is relative to the situation that apoCII is in the same conformation but not bound to the SDS micelle, so that it truly represents the hydrophobic interaction free energy with the SDS micelle. From the hydrophobic free energy ($\Delta G_{\text{hydrophobic}}$) and the thermal energy ($kT = 0.6$ kcal/mol) one can estimate how much the free energy surface is populated as it is governed by the Boltzmann distribution $\exp(-\Delta G_{\text{hydrophobic}}/kT)$. The hydrophobic interaction energy of the complete apoCII is ca. −8 kcal/mol, which corresponds to a binding constant K_b of 10^{-6} M, which is close to experimental estimates with phospholipid vesicles (*64, 65*) or slightly higher than found by Tajima et al., using emulsions of triolein (10^{-7} M, *66*). Note that due to the uncertainty in the estimate of the accessible surface area the absolute value, but not the relative values, of the hydrophobic energies may have to be scaled by as much as a factor of 2.

Helix 3 (class G*) has a similar hydrophobic interaction strength, ca. −2 kcal/mol, as helix 1a, 1b, and 2 (class A). This implies that motion off the surface is as restricted for the helix 3 as for the class A, lipid-binding helices (helices 1 and 2). Thus, this motion is not a feature which distinguishes helix 3 from helices 1 and 2, and we therefore refrain from trying to make a more quantitative estimate of the degree of this motion. The second type of motion, namely, over the surface, does not adversely affect the hydrophobic interaction. It would for that reason be allowed. However, this motion requires that the helices have to pass negatively charged headgroups of the SDS molecules via a concerted retraction of a number of these groups. This would slow the motion, probably beyond the nanosecond time scale (*51*). In addition, this motion is equally likely or unlikely for all three helices and thus neither a distinguishing feature for helix 3. The third type of allowed motion, rolling of the helix around its own axis, is not obstructed by the SDS molecules and could therefore very well be on the nanosecond time scale. Also, the hydrophobic interaction can be maintained over a certain range of roll angle (see below). This motion is therefore the most likely candidate to explain the observed additional nanosecond time scale motion of helix 3. We have considered this motion in more detail via hydrophobic free energy calculations.

As can be seen from Figure 8B, the hydrophobic residues in helix 3 show a reversed Γ-shaped distribution. F67 (as well as V71 and V74 not shown) points in the direction of the hydrophobic moment and toward the interior of the micelle, while L72 and L75 point at an angle of ca −90° to −100° away from F67. Residue I66 (one of the fully conserved residues) points in the opposite direction at an angle of ca. 170°. In contrast, in helix 1 and 2, the hydrophobic residues are all directed toward the micelle surface. Qualitatively, the reversed Γ-shaped distribution means that when the main interaction residues (F67, V71, and V74) are rotated nearly out from the micelle interior (ca. 60° to 90°), the hydrophobic residues L72 and L75 start to interact. Full calculation of the hydrophobic free energy as a function of the roll angle shows that the free energy profile for the helix 3 is indeed relatively wide (from 0° to 100°, Figure 8F), compared to the more steep and narrow interaction profile of helix 1a, 1b, and 2 (from 0° to 20°, Figure 8C−E). From the S^2s of 0.55 one estimates a half angle for helix rotation of ca. 40° for helix 3 and from the S^2s of 0.8 one estimates a half angle of ca. 15° for helix 1a/b and 2 (*63*). We subsequently investigated whether this motion is consistent with the experimental NMR constraints (NOEs, *J*-couplings). Helix 3 was rotated as a unit and residues 57−63 were allowed to adjust during a short restraint SA protocol. We observed that the NOE energy is the most sensitive parameter and remains at a minimum from −60° up to 50°. Consequently, the NMR constraints together with the hydrophobic free energy allow for a rolling motion of helix 3 from 0° to 50°. In contrast, the rolling motion of helix 1a/b and 2 is restricted to ca. 20°.

Support for functional significance of this additional rolling motion of helix 3 comes from the observation that the reversed Γ-shaped distribution of hydrophobic residues is conserved in apoCII from man to fish. First, the main hydrophobic interaction residue in human apoCII, F67, is functionally conserved (67: F or L) as well as the other two lipid-interacting residues 71 and 74 (71: L or V; 74: L or I, V, M, W). Residues 72 and 75, constituting the upper part of the reversed Γ-distribution, are also functionally conserved. They are hydrophobic (72: L or F; 75: L or W), except in chicken and trout apoCII, where one finds the indiscriminate type Y at position 72.

Activation Mechanism. Despite the long history of studies of apoCII, the molecular mechanism for the activation of LPL has remained unknown due to the complexity of the system consisting of apoCII, LPL, and water-insoluble aggregated substrates and detergent-like products (fatty acids). Before discussing the possible significance of the findings in the present study for further understanding the activation mechanism, it is of value to briefly iterate the main findings from previous studies.

Clarke and Holbrook (*67*) found that apoCII and LPL form a 1:1 complex both in solution and in the presence of lipid (one apoCII per subunit in the LPL dimer). The K_d was estimated to 0.2×10^{-6} M in solution, but was clearly decreased in the presence of a lipid surface (10^{-8} M). The association constants in the absence of lipid were nearly the same for apoCII fragments 44−79, 51−79, 56−79, and 61−79, while the one for fragment 65−79 was 10 times lower (*68*). These data show that the fragment 61−79 is long enough for optimal binding to LPL. On the other hand, fragment 56−79 was found to fully stimulate LPL, while fragment 61−79 activates only to 10% (*15*). Under most in vitro conditions apoCII is not needed for the actual binding of LPL to the lipid/water interface (*69*). Direct measurements showed that LPL is in fact more surface active than apoCII (*70*). In optimized systems, the main effect of apoCII is therefore to increase V_{max} with little or no change in the apparent K_m (*69*). The activation by apoCII is specific in the sense that no other peptides than those derived from apoCII activate LPL, but there is no species specificity in the activation. Apo CII from chicken and trout can activate mammalian LPL (*18*, *19*). Exactly what parts of LPL are engaged in the interaction with apoCII is not known. There is evidence for interaction both with the N-terminal folding domain of LPL containing the active site (*71*), as well as with the end of the C-terminal folding domain (*72*). Hill et al. (*72*) proposed that apoCII could bridge from the C-terminal domain of one LPL subunit to the N-terminal domain in the other antiparallel subunit in the LPL dimer. From a number of kinetic studies, it has been concluded that apoCII changes the orientation of the enzyme at the lipid/water interface such that individual lipid molecules more easily can enter (or leave) the active site (*68*, *72*). The effect of apoCII becomes increasingly important with substrates containing long acyl chains (*73*). With short-chain substrates such as tributyrin, there is no effect of apoCII, because the activity of LPL itself is relatively high (*74*). The mobility of longer chain triglycerides within the interface is more restricted than for short triglycerides. Thus, apoCII may activate by facilitating the entry of lipid from the ordered interface to the catalytic site of LPL, as short chains may be able to move by themselves (*73*).

Taken together, all present information indicates that binding to LPL and activation is located at helix 3 in apoCII and/or at residues just prior to this helix. The residues that are evolutionary fully conserved in apoCII, and essential for activation as shown by site-directed mutagenesis, are Tyr63, Ile66, Asp69, and Gln70 (Figure 8B). These residues are all exposed to the solvent and remain so even with the 50°-domain motion of the helix 3. They, thus, form a potential interaction surface for LPL. Residue Ile66 is of particular interest because it is fully conserved, strongly hydrophobic, and mutation of it almost completely abolishes activation (*20*). Thus, this residue could provide specificity and strength in the apoCII−LPL interaction. Hydrophobic faces along the sides of helix 3 are created on the one side by residues Leu72, Leu75, and Gly65 and on the other side by residues Phe67, Val74, and Leu71, which may help guide the substrate molecules toward the active site. The possibility of helix 3 to undergo a rolling motion on the nanosecond time scale could be significant in this process. The hydrophobic residues on apoCII might alternatively dip in and move out of the lipid interface and thereby help to move individual substrate molecules out toward the active site. Interestingly, all the mentioned hydrophobic residues are functionally conserved in the presently known apoCII sequences, with the exception for the chicken and trout sequences. They have a Leu72 to Tyr replacement, indicating that the role of this residue might not be crucial.

Many aspects of the activation mechanism remain unknown, and the proposed mechanism needs experimental verification, e.g., by additional mutagenesis coupled to continued structural and functional studies. Also, the final localization of the apoCII-binding site on LPL is crucial to establish the details of the activation mechanism. A surface on LPL should exist that matches the fingerprint pattern on apoCII.

ACKNOWLEDGMENT

We greatly appreciate the help with the N-terminal amino acid sequence analyses by Dr. Per-Ingvar Ohlsson.

SUPPORTING INFORMATION AVAILABLE

Table with comparison of our N_H and H_N resonance assignments of MacRail et al. (*25*) and our work. Table with ^{15}N relaxation data (T_1, T_2, NOE) measured at 600 and 400 MHz. Two tables with results of analysis of relaxation data including exchange broadening, the residue-specific overall tumbling time corrected for internal motion and normalized, and T_1 ratios at the two magnetic fields. Three figures showing, as function of residue number, time scales for internal motion, the exchange broadening, and the residue-specific overall tumbling time corrected for internal motion. Validation of the final global fold of apoCII−SDS micelle complex via hydrodynamic calculation includes one figure comparing the back-calculated and experimental residue-specific overall tumbling time. This material is available free of charge via the Internet at http://pubs.acs.org.

REFERENCES

1. Breslow, J. L. (1993) Genetics of lipoprotein disorders. *Circulation 87*, III, 16−21.
2. Segrest, J. P., Garber, D. W., Brouillette, C.G., Harvey, S. C., and Anantharamaiah, G. M. (1994) The amphipathic α-helix: A multifunctional structural motif in plasma lipoproteins. *Adv. Protein Chem. 45*, 303−369.
3. La Rosa, J. C., Levy, L. I., Herbert, P., Lux, S. E., and Fredrickson, D. S. (1970) A specific apolipoprotein activator for lipoprotein lipase. *Biochem. Biophys. Res. Commun. 41*, 57−62.
4. Breckenridge, W. C., Little, J. A, Steiner, G., Chow, A., and Poapst, M. (1978) Hypertriglyceridemia associated with deficiency of apolipoprotein C-II. *N. Engl. J. Med. 298*, 1265−1273.
5. Narayanaswami, V., and Ryan, R. O. (2000) Molecular basis of exchangeable apolipoprotein function *Biochim. Biophys. Acta − Mol. Cell. Biol. Lipids 1483*, 15−36.
6. Breiter, D. R., Kanost, M. R., Benning, M. M., Wesenberg, G., Law, J. H., Wells, M. A., Rayment, I., and Holden, H. M. (1991). Molecular structure of an apolipoprotein determined at 2.5-Å resolution. *Biochemistry 30*, 603−608.
7. Borhani, D. W., Rogers, D. P., Engler, J. A., and Brouillette, C. G. (1997) Crystal structure of truncated human apolipoprotein A-I suggests a lipid-bound conformation. *Proc. Natl. Acad. Sci. U.S.A. 94*, 12291−12296.
8. Wilson, C., Wardell, M. R., Weisgraber, K. H., Mahley, R. W., and Agard, D. A. (1991) Three-dimensional structure of the LDL receptor-binding domain of human apolipoprotein E. *Science 252*, 1817−1822.
9. Wang, G., Treleaven, W. D., and Cushley, R. J. (1996) Conformation of human apolipoprotein A-I (166−185) in the presence of sodium dodecyl sulfate or dodecylphosphocholine by ^{1}H NMR and CD. Evidence for specific peptide-SDS interactions. *Biochim. Biophys. Acta 1301*, 174−184.
10. Okon, M., Frank, P. G., Marcel, Y. L., and Cushley, R. J. (2002) Heteronuclear NMR studies of human serum apolipoprotein AI. Part I. Secondary structure in lipid-mimetic solution. *FEBS Lett. 517*, 139−143.
11. Wang, G., Pierens, G. K., Treleaven, W. D., Sparrow, J. T., and Cushley, R. J. (1996) Conformations of human apolipoprotein E(263−286) and E(267−289) in aqueous solutions of sodium dodecyl sulfate by CD and ^{1}H NMR. *Biochemistry 35*, 10358−10366.
12. Fisher, C. A., Wang, J., Francis, G. A., Syskes, B. D., Kay, C. M., and Ryan, R. O. (1997) Bacterial overexpression, isotope enrichment, and NMR analysis of the N-terminal domain of human apolipoprotein E. *Biochem. Cell Biol. 75*, 45−53.
13. Buchko, G. W., Wang, G., Pierens, G. K., and Cushley, R. J. (1996) Conformational studies of an amphipathic peptide corresponding to human apolipoproetin A-II residues 18−30 with a C-terminal lipid binding motif EWLNS. *Int. J. Pept. Protein Res. 48*, 21−30.
14. Rozek, A., Buchko, G. W., and Cushley, R. J. (1995) Conformation of two peptides corresponding to human apolipoprotein C-I residues 7−24 and 35−53 in the presence of sodium dodecyl sulfate by CD and NMR spectroscopy. *Biochemistry 34*, 7401−7408.
15. Kinnunen, P. K. J., Jackson, R. L., Smith, L. C., Gotto, A. M., Jr., and Sparrow, J. T. (1977) Activation of lipoprotein lipase by native and synthetic fragments of human plasma apolipoprotein C-II. *Proc. Natl. Acad. Sci. U.S.A. 74*, 4848−4851.
16. Sparrow, J. T., and Gotto, A. M., Jr. (1980) Phospholipid binding studies with synthetic apolipoprotein fragments. *Ann. N. Y. Acad. Sci. 348*, 187−208.
17. Olivecrona, G., and Beisiegel, U. (1997) Lipid binding of apolipoprotein CII is required for stimulation of lipoprotein lipase activity against apolipoprotein CII-deficient chylomicrons. *Arterioscler. Thromb. Vasc. Biol. 17*, 1545−1549.
18. Andersson, Y., Nilsson, S., Lindberg, A., Thelander, L., and Olivecrona, G. (1996) Apolipoprotein CII from chicken (*Gallus domesticus*) − the amino-terminal domain is different from corresponding domains in mammals. *J. Biol. Chem. 271*, 33060−33066.
19. Shen, Y., Lindberg, A., and Olivecrona, G. (2000) Apolipoprotein CII from rainbow trout (*Oncorhynchus mykiss*) is functionally active but structurally very different from mammalian apolipoprotein CII. *Gene 254*, 189−198.
20. Shen, Y., Lookene, A., Nilsson, S., and Olivecrona, G. (2002) Functional analyses of human apolipoprotein CII by site-directed mutagenesis. Identification of residues important for activation of lipoprotein lipase. *J. Biol. Chem. 277*, 4334−4342.
21. Lycksell, P.-O., Öhman, A., Bengtsson-Olivecrona, G., Johansson, L. B.-Å., Wijmenga, S. S., Wernic, D., and Gräslund, A. (1992) Sequence specific ^{1}H NMR assignments and secondary structure of a carboxy-terminal functional fragment of apolipoproetin CII. *Eur. J. Biochem. 205*, 223−231.
22. Öhman, A., Lycksell, P.-O., and Gräslund, A. (1993) A refined three-dimensional solution structure of a carboxy terminal fragment of apolipoproetin CII. *Eur. Biophys. J. 22*, 351−357.
23. Storjohann, R., Rozek, A., Sparrow, J. T., and Cushley, R. J. (2000) Structure of a biologically active fragment of human serum apolipoprotein C−II in the presence of sodium dodecyl sulfate and dodecylphosphocholine. *Biochim. Biophys. Acta 1486*, 253−264.
24. Hatters, D. M., MacPhee, C. E., Lawrence, L. J., Sawyer, W. H., and Howlett, G. J. (2000) Human apolipoproetin C−II forms twisted amyloid ribbons and closed loops. *Biochemistry 39*, 8276−8283.
25. MacRaild, C. A., Hatters, D. M., Howlett, G. J., and Gooley, P. R. (2001) NMR structure of human apolipoprotein C−II in the presence of sodium dodecyl sulfate. *Biochemistry 40*, 5414−5421.
26. Papavoine, C. H. M., Christiaans, B. E. C., Folmer, R. H. A., Konings, R. N. H., and Hilbers, C. W. (1998) Solution structure of the M13 major coat protein in detergent micelles: A basis for a model of phage assembly involving specific residues. *J. Mol. Biol. 282*, 401−419.
27. Papavoine, C. H. M., Remerowski, M. L., Horstink, L. M., Konings, R. N. H., Hilbers, C. W., and van deVen, F. J. M. (1997) Backbone dynamics of the major coat protein of bacteriophage M13 in detergent micelles by N-15 nuclear magnetic resonance relaxation measurements using the model-free approach and reduced spectral density mapping. *Biochemistry 36*, 4015−4026.
28. Eccles, C., Guntert, P., Billeter, M., and Wuthrich, K. (1991) Efficient analysis of protein 2D NMR spectra using the software package EASY. *J. Biomol. NMR 1*, 111−130.

29. Sattler, M., Schleucher, J., and Griesinger, C. (1999) Heteronuclear multidimensional NMR experiments for the structure determination of proteins in solution employing pulsed field gradients. *Prog. Nucl. Magn. Reson. Spectrosc. 34*, 93−158.
30. Kay, L. E., Keifer, P., and Saarinen, T. (1992) Pure Absorption gradient enhanced heteronuclear single quantum correlation spectroscopy with improved sensitivity. *J. Am. Chem. Soc. 114*, 10663−10665.
31. Schleucher, J., Schwendinger, M., Sattler, M., Schmidt, P., Schedletzky, O., Glaser, S. J., Sorensen, O. W., and Griesinger, C. (1994) A general enhancement scheme in heteronuclear multidimensional NMR employing pulsed-field gradients. *J. Biomol. NMR 4*, 301−306.
32. Larsson, G., Wijmenga, S. S., and Schleucher, J. (1999) A high-resolution HCANH experiment with enhanced sensitivity via multiple-quantum line narrowing. *J. Biomol. NMR 14,* 169−174.
33. Montelione, G. T., Lyons, B. A., Emerson, S. D., and Tashiro, M. (1992) An efficient triple resonance experiment using ^{13}C isotropic mixing for determining sequence-specific resonance assignment of isotropically enriched proteins. *J. Am. Chem. Soc. 114*, 10974−10975.
34. Vuister, G. W., and Bax, A. (1993) Quantitative J correlation − A new approach for measuring homonuclear three-bond $J_{HNH\alpha}$ coupling-constants in N-15 enriched proteins. *J. Am. Chem. Soc. 115*, 7772−7777.
35. Grzesiek, S., and Bax, A. (1992) An efficient experiment for sequential backbone assignment of medium-sized isotopically enriched proteins. *J. Magn. Reson. 99*, 201−207.
36. Grzesiek, S., and Bax, A. (1992) Correlating backbone amide and side-chain resonances in larger proteins by multiple relayed triple resonance NMR. *J. Am. Chem. Soc. 114*, 6291−6293.
37. Larsson, G., Schleucher, J., Onions, J., Hermann, S., Grundström, T., and Wijmenga, S. S. (2002) Backbone Dynamics of a symmetric Calmodulin dimer in complex with the calmodulin-binding domain of the basic-Helix-Loop-Helix transcription factor SEF2−1/E2−2 − A highly dynamic complex. *J. Mol. Biol. submitted*.
38. Farrow, N. A., Muhandiram, D. R., Singer, A. U., Pascal, S. M., Kay, C. M., Gish, G., Shoelson, S. E., Pawson, T., Forman-Kay, J. D., and Kay, L. E. (1994) Backbone dynamics of a free and phosphopeptide-complexed Src-2 homology domain studied by ^{15}N relaxation. *Biochemistry 33,* 5984−6003.
39. Fischer, M. W. F., Majumdar, A., and Zuiderweg, E. R. P. (1998) Protein NMR relaxation: theory, application and outlook. *Prog. Nucl. Magn. Reson. Spectrosc. 33*, 207−272.
40. Grzesiek, S., and Bax, A. (1993) The importance of not saturating H_2O in protein NMR. Application to sensitivity enhancement and NOE measurements. *J. Am. Chem. Soc. 115*, 12593−12594.
41. Piotto, M., Saudek, V., and Sklenar, V. (1992) Gradient-tailored excitation for single-quantum NMR-spectroscopy of aqueous solutions. *J. Biomol. NMR 6*, 661−665.
42. Viles, J. H., Duggan, B. M., Zaborowski, E., Schwarzinger, S., Huntly, J. J. A., Kroon, G. J. A., Dyson, H. J., and Wright, P. E. (2001) Potential Bias in NMR Relaxation Data Introduced by Peak Intensity Analysis and Curve Fitting Methods. *J. Biomol. NMR 21*, 1−9.
43. Larsson, G., Martinez, G., Schleucher, J., and Wijmenga, S. S. (2002) Detection of nanosecond time scale internal motion and determination of overall tumbling times independent of the time scale of internal motion in proteins from ^{15}N relaxation data. *J. Am. Chem. Soc.*, submitted.
44. Brunger, A. T. (1993) X-PLOR Version 3.1: A system for X-ray crystallography and NMR Yale University Press, New Haven.
45. Borgias, B. A., and James, T. L. (1990) MARDIGRAS. *J. Magn. Reson. 87*, 475−487.
46. Folmer, R. H. A., Nilges, M., Papavoine, C. H. M., Harmsen, B. J. M., Konings, R. N. H., and Hilbers, C. W. (1997) Refined structure, DNA binding studies, and dynamics of the bacteriophage Pf3 encoded single-stranded DNA binding protein. *Biochemistry 36*, 9120−9135.
47. Wishart, D. S., Bigam, C. G., Holm, A., Hodges, R. S., and Sykes, B. D. (1995) ^{1}H, ^{13}C and ^{15}N random coil NMR chemical shifts of common amino acids. Investigation of nearst-neighbour effects. *J. Biomol. NMR 5*, 67−81.
48. Nilges, M., Gronenborn, A. M., Brunger, A. T., and Clore, G. M. (1988) Determination of three-dimensional structures of proteins by simulated annealing with interproton distance restraints − Application to crambin, potato carboxypeptidase inhibitor and barley serine proteinase inhibitor-2. *Protein Eng. 2*, 27−38.
49. Brooks, B. R., Bruccoleri, R. E., Olafson, B. D., States, D. J., Swaminathan, S., and Karplus, M. (1983) CHARMM: A Program for Macromolecular Energy, Minimization, and Dynamics Calculations. *J. Comput. Chem. 4*, 187−194.
50. Itri, R., and Amaral, L. Q. (1991) Distance Distribution Function of Sodium Dodecyl Sulfate Micelles by X-ray Scattering. *J. Phys. Chem. 95*, 423−427.
51. Israelachvili, J. (1991) *Intermolecular and Surface Forces* Academic Press, San Diego, Chapter 17.
52. MacKerrel, A. D., Jr. (1995) Molecular Dynamics Simulation of a Sodium Dodecyl Sulfate Micelle in Aqueous Solution: Decreased Fluidity of the Micelle Hydrocarbon Interior. *J. Phys. Chem. 99*, 1846−1855.
53. Har'El Z. Uniform Solution for Uniform Polyhedra, Department of Mathematics, Technion-Israel Institute of Technology, Haifa, 1992. 1992.
54. Christopher, J. A., Swanson, R., and Baldwin, T. O. (1996) Algorithms for Finding the Axis of a Helix: Fast Rotational and Parametric Least-Squares Methods. *Comput. Chem. 20*, 1−27.
55. Eisenberg, D., Weiss, R. M., and Terwilliger, T. C. R. (1984) The hydrophobic moment detects periodicity in protein hydrophobicity. *Proc. Natl. Acad. Sci. U.S.A. 81*, 140−144.
56. Eisenberg, D., Schwarz, E., Komaromy, M., and Wall, R. (1984) Analysis of membrane and surface protein sequences with the hydrophobic moment plot. *J. Mol. Biol. 179*, 125−142.
57. Kyte, J., and Doolittle, R. F. (1982) A simple method for displaying hydrophatic character of a protein. *J. Mol. Biol. 157*, 105−132.
58. Eisenberg, D., and McLachlan, A. D. (1986) Solvation energy in protein folding and binding. *Nature 319*, 199−203.
59. Korzhnev, D. M., Billeter, M., Arseniev, A. S., and Orekhov, V. Y. (2001) NMR study of brownian tumbling and internal motions in proteins. *Prog. Nucl. Magn. Reson. Spectrosc. 38*, 197−266.
60. Milik, M., and Skolnick, J. (1993) Insertion of Peptide Chains into Lipid Membranes: An Off-Lattice Monte Carlo Dynamics Model. *PROTEINS*: *Struct.*, *Funct.*, *Genet. 15*, 10−25.
61. Efremov, R. G., Volynsky, P. E., Nolde, D. E., Vergoten, G., and Arseniev, A. S. (2001) Implicit two-phase solvation model as a tool to assess conformation and energetics of proteins in membrane-mimetic media. *Theor. Chem. Acc. 106*, 48−54.
62. Jarvet, J., Zdunek, J., Damberg, P., and Gräslund, A. (1997) Three-dimensional Structure and Postion of Porcine Motilin in Sodium Dodecyl Sulfate Micelles Determined by 1H NMR. *Biochemistry 36,* 8153−8163.
63. Lipari, G., and Szabo, A. (1982) Model-Free approach to the interpretation of nuclear magnetic resonance relaxation in macromolecules. 1. Theory and range validation. *J. Am. Chem. Soc. 104*, 4546−4559.
64. Cardin, A. D., Jackson, R. L., and Johnson, J. D. (1982) 5-dimethylaminonaphthalene-1-sulfonyl 3-aminotyrosyl apolipoprotein C−III. Preparation, characterization, and interaction with phospholipid vesicles. *J. Biol. Chem. 257*, 4987−4992.
65. McLean, L. R., and Jackson, R. L. (1985) Interaction of lipoprotein lipase and apolipoprotein C−II with sonicated vesicles of 1,2-ditetradecylphosphatidylcholine: Comparison of binding constants. *Biochemistry 24*, 4196−4201.
66. Tajima, S., Yokoyama, S., and Yamamoto, A. (1983) Effect of lipid particle size on association of apolipoproteins with lipid. *J. Biol. Chem. 258*, 10073−11182
67. Clarke, A. R., and Holbrook, J. J. (1985) The mechanism of activation of lipoprotein lipase by apolipoprotein C-II. The formation of a protein−protein comples in free solution and at a triacylglycerol/water interface. *Biochim. Biophys. Acta 827*, 358−368.
68. Voyta, J. C., Vainio, P., Kinnunen, P. K. J., Gotto, A. M., Jr., Sparrow, J. T., and Smith, L. C. (1983) Interaction of synthetic *N*-5-dimethylaminonaphthalene-1-sulfonyl-apolipoprotein C−II peptides with lipoprotein lipase. *J. Biol. Chem. 258*, 2934−2939.
69. Bengtsson, G., and Olivecrona, T. (1980) Lipoprotein lipase: Some effects of activator proteins. *Eur. J. Biochem. 106*, 549−555.
70. Vainio, P., Virtanen, J. A., Kinnunen, P. K. J., Voyta, J. C., Smith, L. C., Gotto, A. M., Jr., Sparrow, J. T., Pattus, F., and Verger, R. (1983) Action of lipoprotein lipase on phospholipid monolayers. Activation by apolipoprotein C-II. *Biochemistry 22*, 2270−2275.
71. Dichek, H. L., Parrott, C., Ronan, R., Brunzell, J. D., Brewer, H. B., Jr., and Santamarina-Fojo, S. (1993) Functional characterization of a chimeric lipase genetically engineered from human lipoprotein lipase and human hepatic lipase. *J. Lipid Res. 34*, 1393−1401.

72. Hill, J. S., Yang, D., Nikazy, J., Curtiss, L. K., Sparrow, J. T., and Wong, H. (1998) Subdomain chimeras of hepatic lipase and lipoprotein lipase. Localization of heparin and cofactor binding. *J. Biol. Chem. 273*, 30929−30984.

73. Shinomiya, M., Jacksson, R. L., and McLean, L. R. (1984) Effect of apolipoproteins C−II on the temperature dependence of lipoprotein lipase-catalyzed hydrolysis of phosphatidylcholines. *J. Biol. Chem. 259*, 8724−8728.

74. Rapp, D., and Olivecrona, T. (1978) Kinetics of milk lipoprotein lipase. Studies with tributyrin. *Eur. J. Biochem. 91*, 379−385.

75. Humphrey, W., Dalke, A., and Schulten, K. (1996) VMD-Visual Molecular Dynamics *J. Mol. Graphics 14.1*, 32−38.

BI0267184